Journal of Laser Applications

RESEARCH ARTICLE | OCTOBER 12 2023

High repetition ultrafast laser ablation of graphite and silicon/graphite composite electrodes for lithium-ion batteries

Alexandra Meyer ; Yannic Sterzl ; Wilhelm Pfleging

J. Laser Appl. 35, 042036 (2023)
https://doi.org/10.2351/7.0001180

Journal of Laser Applications ARTICLE pubs.aip.org/lia/jla

High repetition ultrafast laser ablation of graphite and silicon/graphite composite electrodes for lithium-ion batteries

Cite as: J. Laser Appl. 35, 042036 (2023); doi: 10.2351/7.0001180
Submitted: 14 July 2023 · Accepted: 26 September 2023 ·
Published Online: 12 October 2023

Alexandra Meyer,[a] Yannic Sterzl, and Wilhelm Pfleging

AFFILIATIONS

Institute for Applied Materials—Applied Materials Physics (IAM-AWP), Karlsruhe Institute of Technology (KIT), Hermann-von-Helmholtz-Platz 1, 76344 Eggenstein-Leopoldshafen, Germany

[a]**Author to whom correspondence should be addressed; electronic mail:** alexandra.meyer@kit.edu

ABSTRACT

Laser structuring can be applied to composite electrodes of lithium-ion cells to enhance wetting and to facilitate the usage of thick-film electrodes by reducing the lithium-ion diffusion overpotential and the tortuosity of the electrodes or the usage of electrodes containing silicon, where additional porosity is required to compensate the volume expansion during lithium de-/insertion. To integrate the additional laser processing step in the well-established electrode manufacturing route, the laser processing speed must be significantly increased to match with the belt speed, which is dependent on the electrode thickness and the type of manufacturing route. Upscaling can be realized by increasing the average laser power, laser intensity, and/or laser repetition rate. Here, an ultrashort pulsed laser source with an average power of 300 W and a pulse duration of 600 fs was applied. For the first time, the presented research provides detailed laser ablation processing data for thick-film composite anodes associated with high repetition rates ranging from 4.9 to 48.8 MHz. The patterning results are compared depending on the widths, depths, aspect ratios, the total appearance regarding debris and cracks, and the volume ablation rate. In high repetition rate laser patterning, the subsequent laser pulses interact with the material vapor plasma generated by the previous laser pulses, resulting in lower ablation depths and higher ablation widths. The increase in laser peak intensity leads to higher achievable ablation depths. Processing strategies are identified for two different ablation scenarios focusing on the pouch cells of a Volkswagen ID.3 and the Tesla 4680 cell.

Key words: ultrafast laser ablation, high repetition rates, lithium-ion battery, upscaling, laser structuring, ablation characteristics

I. INTRODUCTION

Lithium-ion batteries are used in electronic devices and electromobility and are in the focus of current research to increase both cell lifetime and capacity. Depending on the intended application, the batteries may be divided into two different types. In high-energy cells, the aim is to maximize gravimetric and volumetric energy density, while high power cells are intended to provide high power densities during cell operation and for fast charging. Electrodes are specially designed according to the application profile. If the cell is to have a high energy density, the proportion of inactive materials must be reduced. This can be achieved by increasing the areal loading of the electrode and, thus, using thick electrode layers while maintaining porosity.[1] To increase the energy density of batteries to over 350 Wh kg^{-1}, which is aspired to be reached by 2025,[2] composite electrodes with thicknesses of more than 100 μm can be utilized as well as high energy materials on both cathodes and anodes. With increasing film thickness, the power density is decreased and high-rate charging or discharging is aggravated.[3] To achieve sufficient performance while using high electrode thicknesses, various laser patterning strategies can be used to introduce artificial porosity, e.g., hole, line, or grid structures.[3] This results in shorter lithium-ion diffusion pathways by reducing the tortuosity and increasing the active surface area, which, in turn, leads to a reduced diffusion overpotential.[1]

Additionally, line structures increase the wettability of electrodes with the liquid electrolyte due to the capillary effect.[4]

Pfleging *et al.*[5] showed that laser patterned channels in NMC cathodes with a thickness of 55 μm improved wetting with the liquid electrolyte due to the capillary effect and increased the specific discharge capacity and lifetime compared to the reference electrode without laser patterning. The shorter wetting time results in a reduction in overall battery manufacturing time as well as a reduction in the associated costs of warm aging and storage, provided structuring can be integrated into the manufacturing process. On the material side, silicon shows promising results to be used as a high capacity anode to increase the energy density of the cell with its theoretical capacity of 3579 mAh g^{-1} when $Li_{15}Si_4$ is formed.[6] Due to the volume change of about 280% during lithiation,[7] the usage of this material in electrodes poses a challenge. The artificial porosity added with laser patterning can reduce or avoid the electrode delamination and crack formation associated with expansion and compression during charging and discharging, which is shown, for example, in Zheng *et al.*[8] They introduced line and grid patterns in silicon/graphite composite electrodes with a thickness of 55 μm and achieved an increase in rate capability and capacity. The increased cracking and film delamination of the unstructured electrodes in comparison to the laser patterned electrodes was also shown. *In situ* scanning electron microscopy images presented in Ref. 9 showed similar behavior for silicon/graphite composite electrodes structured with a line pattern, where delamination could be delayed. Meyer *et al.*[10] introduced line structures in electrodes with an areal capacity of 1.6 mAh cm^{-2} and achieved an increase in lifetime and rate capability. Hole structures were introduced in graphite electrodes by Habedank *et al.*,[11] and cell impedance and charge transfer resistance were reduced, while the specific capacities were increased by about 20% at C/10. Yamada *et al.*[12] recently published a method to structure thin-film graphite and LFP electrodes in a roll-to-roll process with through-holes, and the discharge capacity retention was increased from 60% to 66% and from 76% to 92% at a C-rate of 10 C for LFP and graphite, respectively. Numerous research papers were already published proving the advantageous effects of laser patterning on the cell lifetime, on the specific capacity, and on electrode wetting; a selection of which can be found in Refs. 1, 3, and 13, but the ablation characteristics, which is crucial knowledge to implement this processing step into industrial cell fabrication, have not yet been investigated thoroughly.

An influence on the ablation depth with increasing pulse peak fluence F_{max} according to the logarithmic ablation model established for the ablation of metals[14] was shown in Ref. 15. There, an ultrashort pulsed laser source with a pulse duration of 400 fs that operated at a wavelength of 1040 nm at varying repetition rates (10 Hz to 10 kHz) and a pulse energy with a maximum value of 40 μJ was applied. Hole patterns in graphite electrodes were fabricated and examined in this study. At a constant repetition rate of 10 Hz, as the number of pulses increased, the ablation threshold, achieved by extrapolating the experimental data of the ablation rate, decreased from 13.74 J cm^{-2} at six pulses to 1.92 J cm^{-2} at 100 pulses. The optical penetration depth derived from the logarithmic ablation model decreased as well. Similar to the well-studied laser ablation of metals,[14] the decrease in the ablation threshold laser fluence F_{th} with increasing number of pulses was, therefore, shown for graphite composite electrodes. Furthermore, it was found that when the repetition rate increased while the F_{max} and number of pulses remained constant, the ablation depth decreased. It can be concluded that at high repetition rates, there is an impact on the ablation process due to the interaction of laser pulses with the ablation plume. It can be assumed that plasma shielding effects and laser-induced heat impact have a significant influence.[15] Kouli *et al.*[16] used a laser source operating at a wavelength of 1064 nm, a pulse length of 8.6 ps, and a beam quality factor M^2 of 1.23 to generate hole patterns in two types of double-side coated graphite anodes of different thicknesses (63 and 119 μm). The repetition rate was varied between 40 and 1000 kHz as well as the number of laser pulses (1–25) and the average laser power (12–60 W). As shown in Ref. 15, the ablation depth decreased with an increasing repetition rate and with a decreasing pulse peak fluence. Furthermore, three ablation regimes could be identified. Laser structuring at a structure depth smaller than the coating thickness was characterized by a high ablation rate. If the structure depth is already in the order of magnitude of the layer thickness, interaction with the current collector occurs in addition to the interaction of the laser beam with the coating. This resulted in a decreasing ablation rate and an increasing crater width, measured at the deepest point and at half the depth of the generated hole. Within the third ablation regime a damage of the current collector occurs and structuring of the rear side coating takes place. In addition, Kouli *et al.*[16] observed a bulge around the hole created via ablation with 25 pulses at 1 MHz and a fluence of 0.79 J cm^{-2} with a diameter of 350 μm and a height of 10 μm. It was concluded that thermal effects may occur during ablation at high repetition rates, although a final clarification of the mechanisms for the formation of the bulge is still pending. No one so far has investigated the ablation of electrodes at repetition rates significantly above 1 MHz.

Even though the process of laser patterning seems to be established in research, the implementation of this technology in industry is quite challenging. To introduce the benefits of electrode patterning to commercially manufactured batteries, the patterning must be able to keep pace with the rest of the processes in the manufacturing chain. The electrode coating and drying speeds range from 25 to 85 m min^{-1} using the state of the art wet-film coating,[17,18] depending on the electrode thickness and coating technology. When dry coating with electron-beam curing is used, the coating speed can be increased to 150 m min^{-1} and even up to 300 m min^{-1}.[19–21] With electrostatic spray deposition, coating speed of up to 1.2 m min^{-1} has been achieved.[22] A trade-off between possible achievable patterning speed and quality of the structures must be considered. An appropriate selection of laser and process parameters such as wavelength λ, pulse length τ, laser fluence F, scanning speed v_L, pulse overlap n, and repetition rate f plays a decisive role in laser structuring. The knowledge about the ablation behavior is essential for a successful integration of the process into the production line. Here, the required pulse overlap as well as the necessary pulse peak fluence, i.e., laser power, repetition rate, and beam profile, for ablation with one laser scan are of fundamental interest.

In this work, laser ablation parameter studies for line patterning are carried out on two different electrode types with similar film thicknesses but different compositions, i.e., graphite end

silicon/graphite composite electrodes. In particular, the use of the next generation electrode material silicon is leading the way in increasing the specific capacities on cell level. Laser patterning of this material can enable its establishment in the industry, or the amount of silicon in silicon/graphite composite electrodes can be increased significantly while maintaining the required cell lifetimes. The usage of an ultrashort-pulsed laser source with an elevated power of up to 240 W, high repetition rates of up to 48.8 MHz, fast scanning speed of up to 5 m s^{-1}, and a beam propagation ratio M^2 of 1.1 to ablate the electrode material is of great significance regarding the introduction of electrode laser processing in the industrial manufacturing line. For an aspired upscaling of the structuring process, the applied scanning strategy with one laser scan per line pattern is crucial, enabling a constant strip feed. The generated structures manufactured here are examined regarding the width and depth using digital microscopy and light microscopy. Conclusions for the ablation behavior of electrodes and the introduction of this technology in industrial battery manufacturing can be drawn. An examination of the electrochemical behavior of the laser patterned electrodes was not conducted in this work, as the positive impact of laser patterns on, for example, the (specific) capacity and lifetime of lithium-ion cells was already shown numerous times, extensive research regarding this topic can be found in, e.g., Refs. 1, 3–5, 8, 10, 11, 13, 15, and 23–30.

II. EXPERIMENT

Graphite and silicon/graphite composite electrodes were prepared via ball milling, and the composition thereof is summarized in Table I. The slurry thickener was a water-based 2.5 wt. % sodium carboxymethyl cellulose (CMC, MTI Corporation, USA) solution, which was prepared with a vacuum mixer (MSK-SFM-7, MTI Corporation, USA) and subsequently stirred for 24 h with a magnetic stirrer to achieve homogeneous gelation. The graphite (SPGPT808, Targray Inc., Canada), conductive carbon black (CB, C-nergy Super C65, Imerys G&C, Switzerland), silicon (Targray Inc., Canada), if applicable, and CMC solution were then premixed with a centrifugal mixer (Speedmixer DAC 150 SP, Hauschild, Germany). For complete homogenization, a ball mill (PULVERISETTE 7 premium line, Fritsch, Germany) was utilized. After grinding, balls were removed with a sieve, the binder, and a styrene-butadiene rubber solution with a solid content of 50% (SBR, MTI Corporation, USA) was added and stirred into the mixture with the centrifugal mixer. The electrode slurry was deposited on a copper current collector (9 μm thickness, EQ-bccf-9u-180, MTI Corporation, USA) with a universal applicator (ZUA2000, Zehntner GmbH, Switzerland) and dried at room temperature. The gap height was 450 μm. To reach a calculated porosity of 40%, the electrodes were calendered after drying. The electrode thickness was thereby reduced to approximately 120 μm, being in the range of state-of-the-art graphite electrodes used in the Volkswagen ID.3 with 115.3 μm.[31]

TABLE I. Composition of the graphite and silicon/graphite composite electrodes.

Material	Electrode composition I Mass fraction (wt. %)	Electrode composition II Mass fraction (wt. %)
Graphite	85	80
C65	5	5
CMC	5	5
SBR	5	5
Silicon	—	5

The electrodes were ablated with a high-power, high repetition rate laser source (FX600-2-GFH, EdgeWave GmbH, Germany) operating at a wavelength of 1030 nm, a pulse length of 600 fs, and a maximal average power of 300 W. The raw laser beam provides a waist radius $w_{a,x/y}$ with 1396 and 1279 μm in the x- and y-direction, respectively, with beam propagation ratio $M_x^2 = 1.11$ and $M_y^2 = 1.01$. The laser seeder pulses had a frequency of 48.8 MHz, but by working with a pulse picker, several seeder frequency dividers could be set, which corresponds to ten different pulse repetition rates between 48.8 and 4.9 MHz. To achieve a constant laser pulse overlap and a constant pulse-to-pulse distance of 0.1 μm for the investigation of the ablation behavior of the electrodes, the ratio of the laser scan speed v to the repetition rate f was kept constant at 0.102 μm for most experiments. To use constant pulse energies E_p, different average laser powers P_{avg} between 12 and 120 W were applied, and the repetition rate f was adjusted accordingly,

$$E_p = \frac{P_{avg}}{f} = \text{const.} \quad (1)$$

A comparison of the ablation behavior depending on the repetition rate with a constant pulse peak fluence can be achieved. The SFD, the associated repetition rates, and scanning speeds are summarized in Table II. Additionally, experiments with varying average laser power (up to 240 W) and varying laser scanning speeds were conducted.

The experimental setup was realized in a laser material processing system (PS450-TO, Optec S.A, Belgium). A scanner (IntelliSCAN III 30, SCANLAB GmbH, Germany) and a F-theta lens (S4LFT2430/328, Sill Optics GmbH & Co. KG, Germany) were used, as illustrated in Fig. 1.

A BET with a 2.2-fold expansion was installed at position 1 and a BET with an expansion factor of 2.5 was installed at position 2.

TABLE II. Seeder frequency divider (SFD), repetition rates, and scan speed for each repetition rate.

SFD	Repetition rate (MHz)	Scanning speed (v/mm s^{-1})
1	48.8	5000
2	24.4	2500
3	16.3	1667
4	12.2	1250
5	9.8	1000
6	8.1	833
7	7.0	714
8	6.1	625
9	5.4	556
10	4.9	500

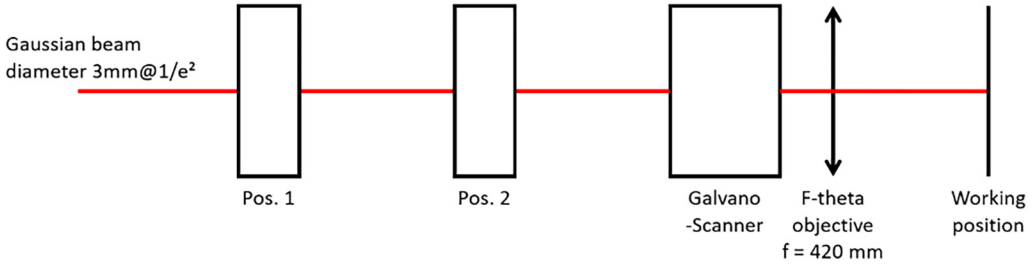

FIG. 1. Schematic view of the applied optical setup including the laser beam, the scanner, and F-theta lens as well as two positions for beam expanding telescopes.

In the focal plane ("working position"), the beam has a calculated dimension of 39.1 μm in the x-direction and 35.9 μm in the y-direction. For each set of parameters, six lines were structured into the electrodes. All experiments were conducted using a unidirectional scanning strategy with a single scan per line. A digital microscope (VHX 5000, Keyence, Japan) was applied for characterization of laser generated grooves. From the created omnifocal panoramic images at a 70× magnification, an average profile was calculated from the depth information of 11 profiles with a distance of 30 μm. From the calculated average profile, the structure depth d as well as the structure width at around 0%–5%, 50%, and 95%–100% of depth, named b_u, b_m, and b_l, respectively, of the six generated channels per parameter set were measured, and the average values as well as the aspect ratios were calculated. The aspect ratio is defined as the ratio of the ablation depth d and the ablation width b_m. A high aspect ratio, corresponding to low mass loss, is aspired. The ablated area A was calculated with the approximation of the grooves as two trapezoids,

$$A = 0.25d \cdot (b_u + 2b_m + b_l). \quad (2)$$

A schematic view of the ablation profile with the two trapezoids is shown in Fig. 2.

Additionally, the structured surfaces were evaluated regarding crack formation, thermal-induced damage, and debris formation with a scanning electron microscope (SEM, Phenom XL, Thermo Fisher Scientific Inc., USA) with an acceleration voltage of 10 kV. A cross-sectional view was evaluated using a different SEM (Philips FEI XL 30S) equipped with an energy-dispersive x-ray spectroscope using an acceleration voltage of 15 kV.

Unstructured electrodes and one selected structured electrode with silicon/graphite as active materials were assembled in CR2032 coin cells versus lithium (0.25 mm thickness, Merck KGaA, Germany) and electrochemically characterized using rate capability measurements. The electrodes were dried at 100 °C for 24 h prior to assembly. The cell assembly was conducted in an argon-filled glovebox (LABmaster pro, M. Braun, Germany) with $H_2O < 0.1$ ppm and $O_2 < 0.1$ ppm. As a separator, a 25 μm thick polypropylene film was used (Celgard, USA). 160 μl electrolyte solution was added, containing 1.3M $LiPF_6$, the solvents ethylene carbonate (EC) and ethyl methyl carbonate with a weight ratio of 3:7 as well as 5 wt. % fluoroethylene carbonate. The cells were sealed using an electric cell crimper (MSK-160D, MTI Corporation, USA). The formation as well as subsequent galvanostatic measurements were conducted using a constant current– constant voltage (CCCV) protocol during discharge and a constant current protocol during charge using a battery cycling system (BT 2000, Arbin Instruments, USA). The cells were cycled in a voltage window between 0.01 and 1.5 V. The rate capability measurement steps are summarized in Table III.

III. RESULTS AND DISCUSSION

A. Ablation depth

Scanning electron microscopy (SEM) images selected structures are shown in Figs. 3(a) and 3(b) for the ablation of graphite and silicon/graphite electrodes at 30 W average laser power, at a repetition rate of 4.8 MHz and a scanning speed of 500 mm s^{-1}. No cracks or debris are visible on the surface of the electrode or at the sidewalls of the grooves. The ablation depths are 108 ± 3 and 107 ± 8 μm, and the widths are 84 ± 4 and 83 ± 6 μm for graphite and silicon/graphite electrodes, respectively. The electrodes have

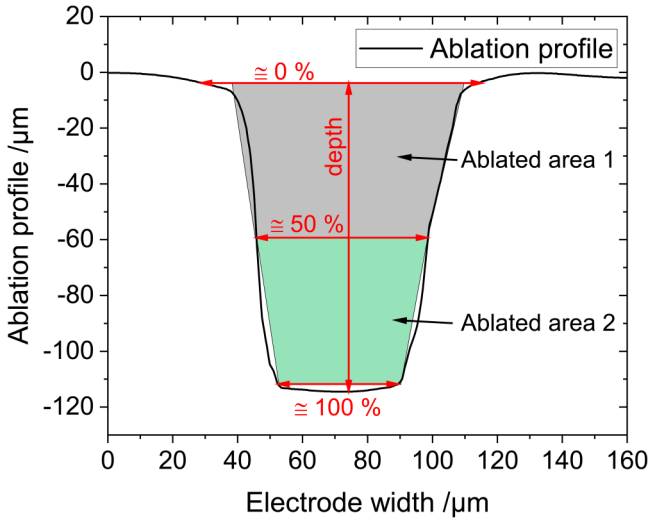

FIG. 2. Schematic view of the measurement positions for different ablation depths.

TABLE III. Formation and measurement steps for the rate capability measurement.

C-rate for CC discharge (h^{-1})	0.05	0.1	0.2	0.5	1	2	3	5
C-rate corresponding to termination current during CV discharge (h^{-1})	0.02	0.05	0.1	0.1	0.1	0.1	0.1	0.1
C-rate for CC charge (h^{-1})	0.05	0.1	0.2	0.5	1	2	3	5
Number of cycles	3	5	5	10	10	10	10	10

very similar characteristics, making them hardly distinguishable. In Fig. 3(c), the scanning electron microscopy image of the graphite electrode structured with 120 W average laser power and a repetition rate of 48.8 MHz with a scanning speed of 5000 mm s^{-1}. The ablation depth is $37 \pm 1\,\mu$m and the width is $82 \pm 3\,\mu$m. Even for the high-power laser ablation, neither cracks nor debris was found on the surface or in the sidewalls of the grooves.

SEM images of a cross-sectional view of one of the grooves manufactured with a laser power of 40 W, a repetition rate of 12.2 MHz, a scanning speed of 1250 mm s^{-1}, and a fluence of 0.56 J cm^{-2} are shown in Fig. 4. The depth was measured to be $58 \pm 3\,\mu$m. An overview of the sample is shown in Fig. 4(a). The electrode was bend in an angle of 90°, and the sidewall of the groove was positioned horizontally to provide a clear view. During the bending process, the electrode broke to expose the laser-unaffected area. It partly detached from the current collector during this process. Figure 4(b) shows a more detailed view, where the sidewall and the broken, not laser patterned parts of the electrodes can be identified. In Fig. 4(c), the upper part of the electrode, i.e., the sidewall of the groove, is displayed. In the detailed view, graphite particles can be identified.

Additionally, a large number of small particles with a size of less than 100 nm are found. It is expected that these particles are formed during laser ablation. After the laser beam vaporizes the material, it will precipitate in the vicinity of the affected area forming nanosized particles, which are no longer graphitic, but amorphous carbon, similar to the already contained carbon black. They, therefore, do not deteriorate the performance of the electrode but rather increase the electric conductivity of the electrode in the grooves. Figure 4(d) shows the lower part of the electrode, where the material was not laser patterned, but broken for the preparation of these SEM images. The large graphite particles can be clearly identified. On top and in between the particles, the smaller nanosized carbon black particles can be found. Energy-dispersive x-ray spectroscopy was performed on the area shown in Fig. 4(b), and no difference in the chemical composition between the upper and the lower part of the electrode, i.e., the patterned and the unaffected area, was measured. The results can be found in Fig. 20. Additional to carbon, sodium, and oxygen, copper was found, being the material of the current collector. Aluminum was found on the surface of the electrode, and the false detection of this material most probably stems from to the angle of 90° from the surface to the detector, resulting in a distortion of the peak. Zirconium was found in small particles throughout the electrode, stemming from abrasions of the milling balls during electrode slurry manufacturing.

The ablation depths of silicon/graphite composite and graphite electrodes as a function of the laser pulse peak fluence are shown in Figs. 5(a) and 5(b). Very similar ablation behaviors are observed for both compositions. At the materials' surface, the laser beam energy is absorbed, and the surface temperature increases. The decomposition temperatures of CMC and SBR are 245[32] and 439.89 °C,[33] respectively, being orders of magnitude lower compared to decomposition temperatures of silicon (melting temperature 1410 °C[34]) or carbon (sublimation at around 3622–3747 °C[35]).

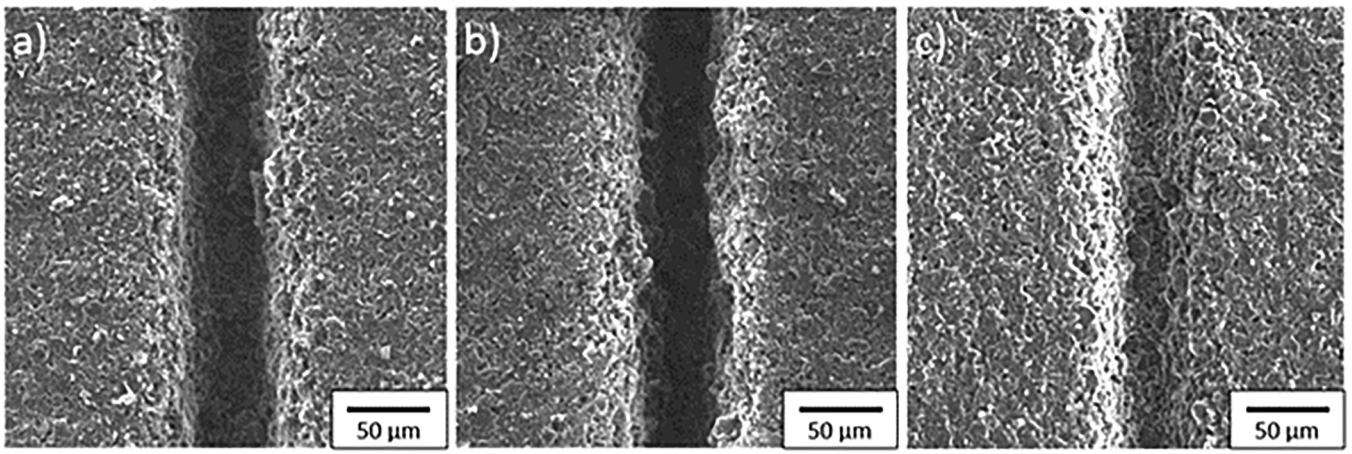

FIG. 3. Scanning electron microscopic images of (a) graphite and (b) silicon/graphite composite electrode structured with 30 W laser power at a repetition rate of 4.9 MHz with a scanning speed of 500 mm s^{-1}. (c) shows the scanning electron microscopy image of the graphite electrode structured with 120 W average laser power and a repetition rate of 48.8 MHz with a scanning speed of 5000 mm s^{-1}.

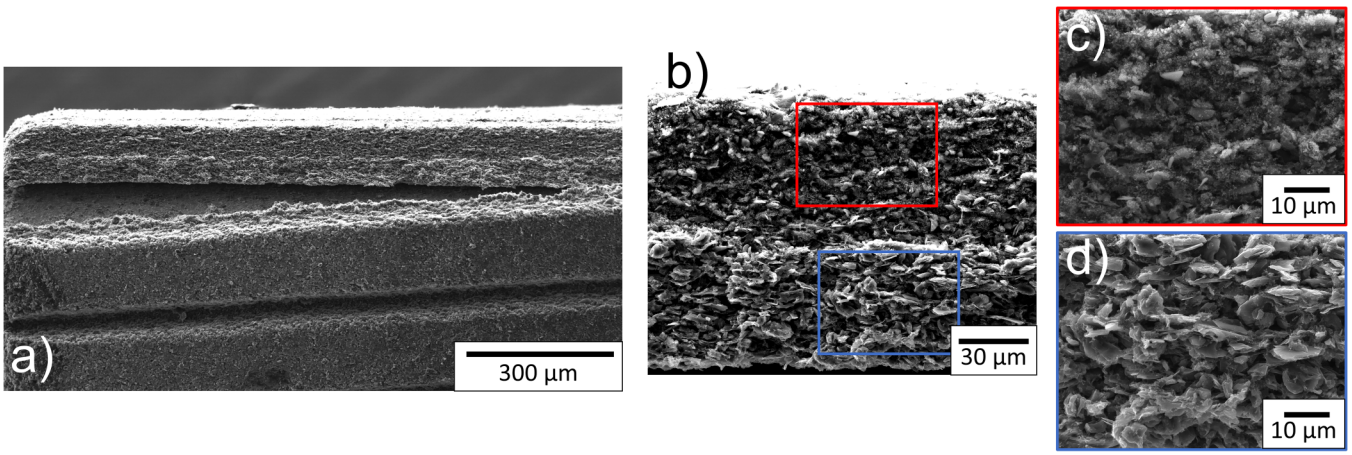

FIG. 4. Scanning electron microscopy image of the groove manufactured with a laser power of 40 W, a repetition rate of 12.2 MHz, and a scanning speed of 1250 mm s^{-1}. An overview of the sample and its position in the SEM is shown in (a); (b) is showing the surface of the groove as well as the not laser patterned electrode. (c) is a detailed view of the surface of the laser patterned area and (d) a detailed view of the unstructured surface, i.e., the cross-sectional view of the electrode accomplished through mechanical breakage.

When the temperature of the material exceeds the binder's decomposition temperatures, they will decompose almost immediately, resulting in a vapor plume, ejecting the graphite, carbon black, and silicon. This was already described in Ref. 4 for composite electrodes or in Ref. 36 for a metal powder in a polymer matrix. Since the ablation results of the silicon/graphite composite and the graphite electrode differ so marginally, only the results of the silicon/graphite composite electrode will be discussed in the following, and the same conclusions can be drawn for the graphite composite electrode. The ablation depths in Figs. 5(a) and 5(b) are characterized by a change in the slope in a range between 0.2 and 0.43 J cm^{-2}. For comparison, a change in the slope as a function of the pulse peak fluence is known for laser-assisted drilling of metals. There, the two ablation regimes in the machining of metals are divided into ablation without thermal influence at low pulse peak fluences and ablation with thermal influence at high pulse peak fluences.[14] However, the ablation characteristics associated with laser drilling cannot be directly transferred to laser direct-write ablation, in which the laser fluence on the substrate surface is not spatially constant due to the pulse offset and the Gaussian distribution of laser intensity, but a change in the slope is still observed. The rather high pulse overlap can be a reason for the observed ablation behavior. Shirk *et al.*[37] determined the ablation threshold for highly oriented pyrolytic graphite to be 0.25 J cm^{-2} (at a pulse length of 120 fs and a wavelength of 825 nm), i.e., a pulse peak fluence in the range of the change in slope in Fig. 5.

In this context, a significant increase in the proportion of ablated graphite could lead to the observed transition in ablation behavior. For laser fluences above approximately 1.5 J cm^{-2}, a saturation effect in the ablation depth can be observed. When the current collector is reached during ablation, the depth cannot be increased further, and the beam is de- or reflected. The role of the binder material in the ablation behavior and threshold fluence of the electrode cannot easily be determined. At sufficiently high fluences, the ablation rates of most polymers are similar.[38] The ablation threshold correlates with the optical bandgaps of the polymers.[38] For fs laser pulses, a multiphoton adsorption is realized with sufficient time overlap, and the absorbed energy density can be increased to exceed the threshold fluence.[38] Ablation threshold fluences for CMC and SBR have not been reported in the literature.

The ablation depths as a function of the repetition rate for constant fluences are shown in Fig. 6 for silicon/graphite electrodes and in Fig. 21 for graphite electrodes. For the lowest constant fluence of 0.21 J cm^{-2}, no impact of the repetition rate on the ablation depth can be found. At higher fluences, a decrease in ablation depth can be found at elevated repetition rates. Due to high repetition rates, laser pulses interact with the ablation plume (material vapor plasma) generated by the preceding laser pulse leading to attenuation and deflection or dispersion of the incident laser beam.

Up until a repetition rate of 24.4 MHz, the ablation depth decreases with increasing repetition rates, while the ablation width increases, see Fig. 9, which is another indication that the laser beam is dispersed and expanded by the material vapor plasma. At the highest repetition rate of 48.8 MHz, both the ablation depth and width are reduced, resulting in a decrease in the amount of the ablated material. The energy density of the incident laser beam is reduced due to dispersion, which is more severe for higher repetition rates; this was already reported for the ablation of polymers with a ps laser source and high repetition rates in Ref. 39. This impact on ablation characteristic is even more severe at elevated fluences (0.84 J cm^{-2}), where the ablation depth decreases from above 100 μm at 4.88 MHz to 60 μm at 48.8 MHz. This is due to the plasma plume properties such as electron density, electron temperature, as well as material vapor density, which reach their critical values with regard to attenuation (i.e., increased plasma absorption coefficient) and dispersion at elevated laser fluences. A well-known critical condition is achieved when the plasma frequency ω_P, which is a function of electron density, reaches values equal or above the

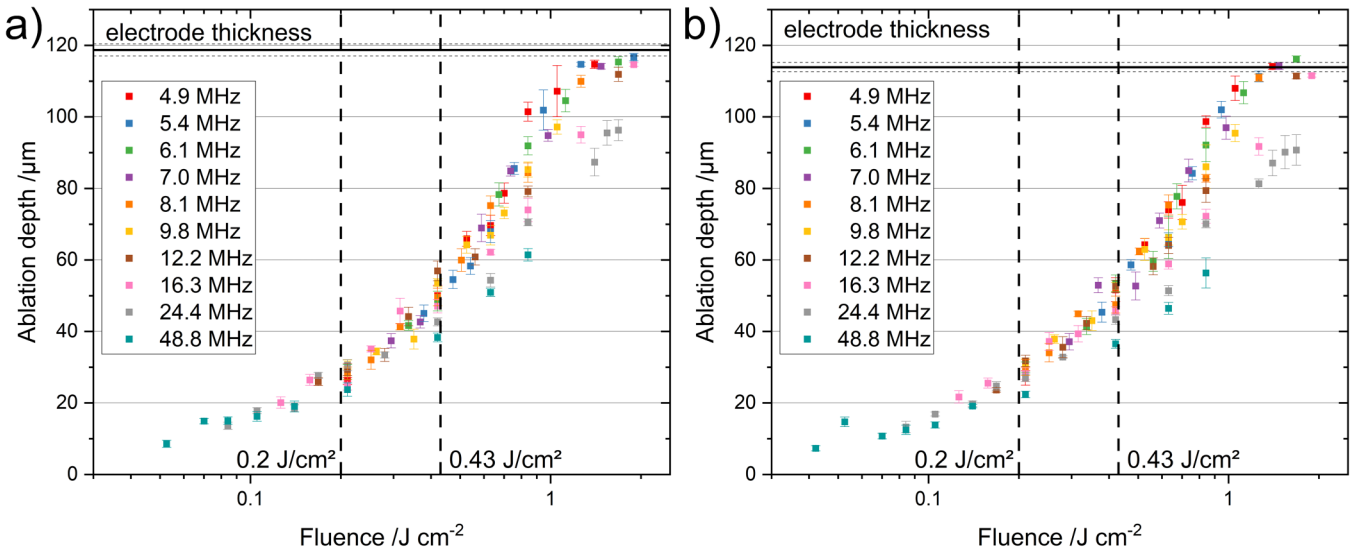

FIG. 5. Ablation depth depending on the pulse peak fluence for (a) silicon/graphite composite electrodes and (b) graphite electrodes, ablated with a fs laser source for different repetition rates and scanning velocities, and a constant pulse-to-pulse distance of 0.1 μm.

optical frequency ω_{Laser} of the incident laser beam, e.g., for high plasma frequencies ($\omega_P > \omega_{\text{Laser}}$), the laser beam will be completely reflected.[40]

An illustrative representation of the ablation depth that is achievable by the process is the plot versus the repetition rate at constant average laser power, since the average laser power and the repetition rate are values directly given to the laser. By keeping the pulse-to-pulse distance constant at 0.1 μm, it is also possible to make a statement about the achievable structuring speed. This can be seen for silicon/graphite composite electrodes in Fig. 7 and for graphite electrodes in Fig. 22. With increasing laser power, higher

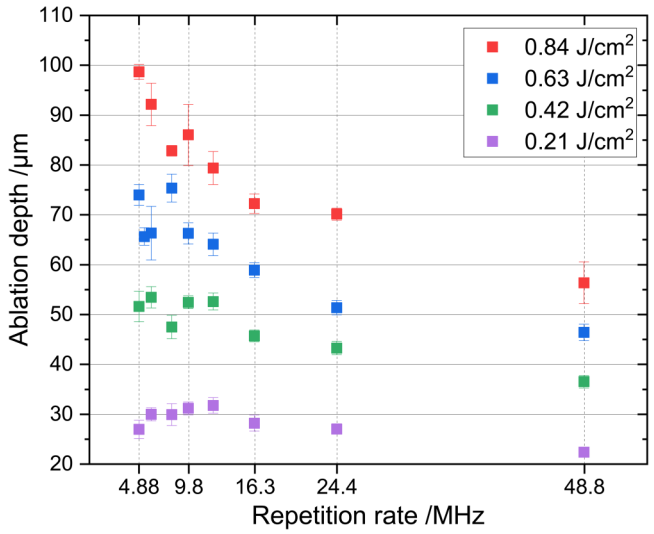

FIG. 6. Ablation depth as a function of repetition rate at constant pulse peak laser fluences for silicon/graphite composite electrodes ablated with a fs laser at different scanning velocities and constant pulse-to-pulse distance of 0.1 μm.

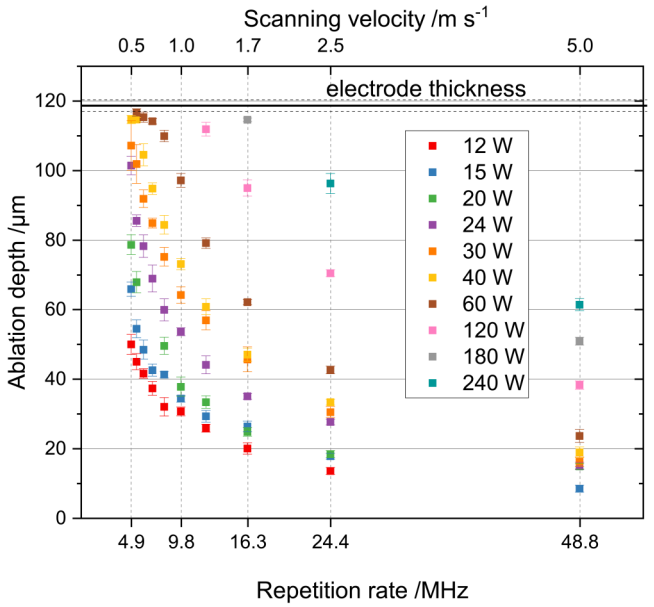

FIG. 7. Ablation depth for constant laser powers as a function of repetition rate or corresponding scanning velocity for silicon/graphite composite electrodes, ablated with a fs laser for different scanning velocities and a constant pulse-to-pulse distance of 0.1 μm.

ablation depths can be achieved, while an increased repetition rate decreases the ablation depth. The copper current collector can be exposed for 40, 60, 180, and 240 W. At a laser power of 60 W, the curve flattens with decreasing repetition rate when the current collector is reached, as it was already described in Ref. 16.

B. Ablation width

The upper ablation width (measured at 0%–5% of ablation depth, see Fig. 2) of the grooves was measured with a digital microscope and is shown in Fig. 8 for silicon/graphite composite electrodes and in Fig. 23 for graphite electrodes. Similar to the ablation depth, the ablation width is characterized by a logarithmic behavior. The narrowest groove structures while the current collector is exposed (marked with open symbols in the figure) can be realized when a pulse peak fluence of 1.4 J cm^{-2} and a repetition rate of 4.9 MHz are being used, with a width of 67.9 ± 2.5 μm. The widest structures while the current collector is reached, measuring 90.3 ± 6.2 μm, are achieved when a repetition rate of 16.3 MHz and a pulse peak fluence of 1.89 J cm^{-2} are applied.

For most fluences, the ablation width increases with increasing repetition rate and decreases again when the maximum repetition rate of 48.8 MHz is applied, which is shown in more detail in Fig. 9 for silicon/graphite composite electrodes and in Fig. 24 for graphite electrodes. For example, the ablation width is measured to be 74.7 ± 4.7 μm for a fluence of 0.84 J cm^{-2} and a repetition rate of 24.4 MHz but can be reduced to measure 59.2 ± 4.1 μm when a repetition rate of 48.8 MHz is applied. The reason for this behavior could be assigned to the time-dependent plasma plume expansion. The plasma velocity of a highly oriented pyrolytic graphite was measured to be in the range between 10 and 30 km s^{-1}.[41] At a

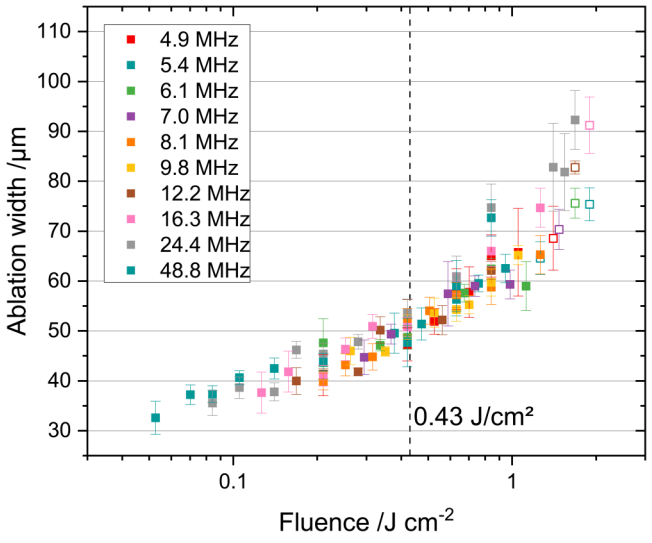

FIG. 8. Upper ablation width depending on the pulse peak fluence for silicon/graphite composite electrodes ablated with a fs laser for different scanning velocities and a constant pulse-to-pulse distance of 0.1 μm. Filled symbols: current collector was not reached; open symbols: current collector was reached.

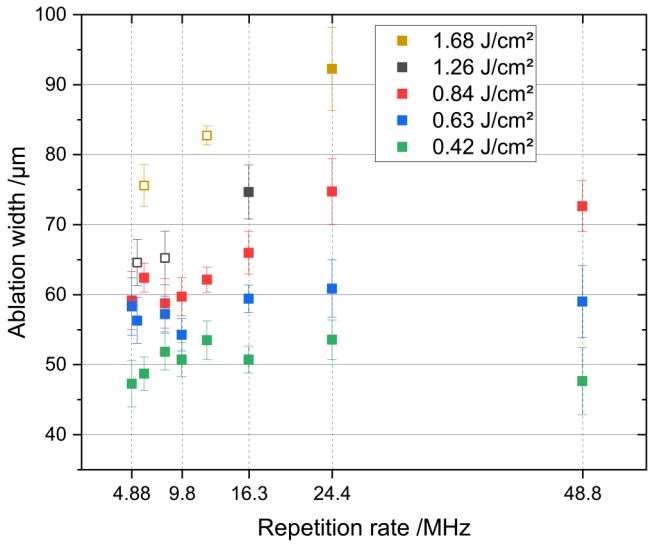

FIG. 9. Upper ablation width depending on the repetition rate for a constant pulse peak fluence for silicon/graphite composite electrodes, ablated with a fs laser for different scanning velocities and a constant pulse-to-pulse distance of 0.1 μm. Solid symbols: current collector was not reached; open symbols: current collector was reached.

repetition rate of 4.9 MHz, the size of the plasma plume is between 2.04 and 6.12 mm when the next laser pulse is fired. With a repetition rate of 48.8 MHz, the plasma has a size between 0.205 and 0.615 mm when the subsequent laser pulse follows. For very high repetition rates, the size of the expanding plasma while getting in contact with the subsequent laser pulse is quite small and the electron density per volume is high. A high electron density leads to a high plasma frequency and, thus, to a high absorption of laser energy in the plasma. The energy density hitting the material surface is quite low leading to a small ablation depth. Due to the small size of the plasma, the dispersion of the laser beam is less pronounced in comparison to a larger plasma plume, thus leading to a slight decrease in ablation crater diameter or structure width. The plasma is the most intense after 5–20 ns.[42] With a temporal distance of 204.08 ns for a repetition rate of 4.9 MHz and 20.49 ns for 48.8 MHz, the effect of the plasma plume is more severe for ablation with higher repetition rates.

The graphs for ablation widths at approx. 50% of the total depth (middle) and at approx. 95% of the total depth (lower) are shown in Figs. 25 and 26 for graphite electrodes and Figs. 27 and 28 for silicon/graphite electrodes. The lower and middle ablation widths behave similarly to the upper ablation width. With increasing pulse peak fluence, the ablation width is increased. For the same pulse peak fluence, the ablation width is increased with increasing repetition rates. A significant increase in the lower ablation width can be observed when the current collector is reached, which can be seen prominently for the repetition rates of 4.9–7 MHz for fluences over 1.26 J cm^{-2} for silicon/graphite composite electrodes in Fig. 28. Exceptions are the repetition rates of 8.1 and 9.8 MHz, since there

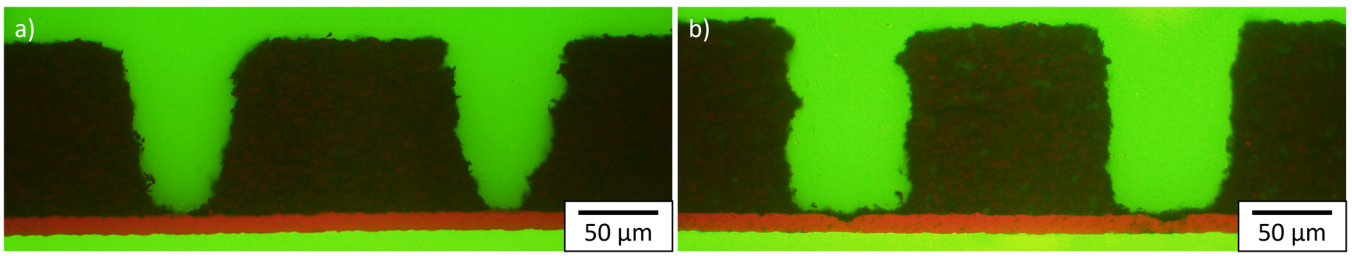

FIG. 10. Light microscopy images of cross sections of the silicon/graphite electrode structured with a repetition rate of 5.4 MHz and a velocity of 0.55 m s^{-1}, pulse-to-pulse distance 0.1 μm: (a) pulse peak fluence of 1.26 J cm^{-2}; (b) pulse peak fluence of 1.89 J cm^{-2}.

the maximum used fluences were 1.26 and 1.05 J cm^{-2}, respectively, and the current collector could not be reached. The same behavior can be observed for graphite electrodes shown in Fig. 26 for repetition rates between 4.9 and 16.3 MHz and fluences larger than 1.26 J cm^{-2}. An exception is the repetition rate of 9.8 MHz, since there the maximum used pulse peak fluence was 1.05 J cm^{-2} and the current collector could not be reached. When the current collector is reached, but the fluence is increased more, which was done for a repetition rate of 5.4 MHz and the fluence of 1.26 and 1.89 J cm^{-2} for silicon/graphite electrodes, more material is ablated. The lower and middle ablation widths are increasing, which can be proven with the cross section analysis shown in Fig. 10.

As soon as the current collector is reached and the copper is exposed, and since copper has an optical reflectance of about 97% for the used wavelength,[43] whereas pure graphite would absorb about 58% of the laser beam intensity,[44] the laser beam is deflected and interacts with the anode material on the interior wall of the grooves, coupling back into the material, resulting in a total absorption of nearly 100% due to the topography of the electrodes. This results in further ablation and an increase in the width of the grooves, which is more pronounced at the lower and middle measuring position. Similar ablation behavior was observed for the patterning of LFP cathodes[45] and graphite electrodes.[16]

The equation for describing the laser fluence is

$$F(r) = F_{\max} \cdot \exp\left(-\frac{2r^2}{w_f^2}\right), \tag{3}$$

with w_f being the beam waist and r being the radial distance from the center axis of the beam, and the equation for the ablation depth per pulse is[14]

$$d \approx \delta \cdot \ln\left(\frac{F(r)}{F_{\text{th}}}\right), \tag{4}$$

with δ being the optical penetration depth and $d(r = b) = 0$ for the ablation crater width b; the ablation threshold F_{th} can be determined by linear regression when the squared upper ablation width b^2 is plotted against the logarithm of the pulse peak fluence $F_{\max}$ according to the following equation, similar to:[46]

$$b^2 = 2 \cdot w_f^2 \cdot \ln\left(\frac{F_{\max}}{F_{\text{th}}}\right). \tag{5}$$

The beam waist in the focal plane is given as an approximation of the mean value of the two ellipse radii (19.3 μm). The standard deviations of the ablation widths are not considered in this calculation. Since a change in the ablation regime is observed for fluences larger than 0.43 J cm^{-2}, the ablation threshold is only calculated for fluences smaller than this value. The ablation threshold can be determined to be 14.9 ± 0.9 mJ cm^{-2} for silicon/graphite composite electrodes and 10.6 ± 0.7 mJ cm^{-2} for graphite electrodes. The associated graphs can be found in Figs. 11 and 29. The global R^2 is 0.697 85 for graphite electrodes and 0.643 02 for silicon/graphite composite electrodes. According to Eq. (6), a

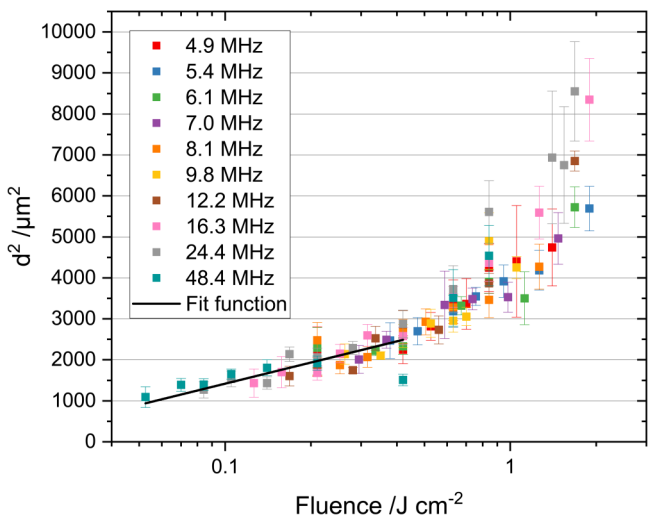

FIG. 11. Squared upper ablation width and fitting function for pulse peak fluences smaller than 0.43 J cm^{-2} depending on the repetition rate for constant pulse peak fluence for silicon/graphite composite electrodes ablated with a fs laser at different scanning velocities and a constant pulse-to-pulse distance of 0.1 μm.

change in ablation width can only occur with a change in beam waist if the logarithmic ablation law is valid. Therefore, the change in slope of $b^2(F_{max})$ for peak fluences above 0.43 J cm^{-2}, as indicated by Fig. 9, is due to a change in the ablation process mechanism. Due to the repetition rate in the MHz regime and a typical lifetime of laser-generated plasma plume in the μs regime, it is assumed that at elevated laser fluences—similar to an increase in the repetition rate—the impact on electron density and plasma temperature becomes increasingly important leading to an enforced gradient in electron density and, thus, to a dispersion of the incident laser beam resulting in an increase in structure width b.

C. Aspect ratio

The aspect ratios as a function of the pulse peak fluence are shown in Fig. 12 and in Fig. 30 for silicon/graphite and graphite composite electrodes, respectively. The aspect ratio is increasing with increasing fluence, until a maximum is reached. When the current collector is exposed, the aspect ratio is decreasing with increasing fluence. The highest aspect ratio can be achieved for a repetition rate of 4.9 MHz and a pulse peak fluence of 1.05 J cm^{-2}.

The aspect ratio depending on the repetition rate for constant fluences is shown in Fig. 13 and in Fig. 31 for silicon/graphite and graphite electrodes, respectively. With increasing repetition rate, the aspect ratio decreases for all fluences, while this behavior is most pronounced at elevated fluences, e.g., 0.84 J cm^{-2}. To reach high aspect ratios, the fluence should, therefore, be chosen with respect to the electrode film thickness, and lower repetition rates should be preferred.

Similar to Fig. 7, the aspect ratio can also be plotted depending on the repetition rate or the scanning velocity for constant laser

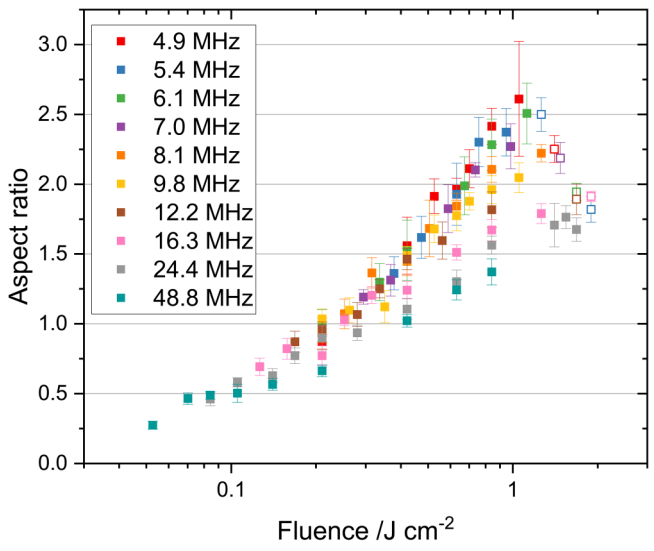

FIG. 12. Aspect ratio of the grooves depending on the pulse peak fluence generated in silicon/graphite composite electrodes, ablated with a fs laser for different scanning velocities and a constant pulse-to-pulse distance of 0.1 μm. Solid symbols: current collector was not reached; open symbols: current collector was reached.

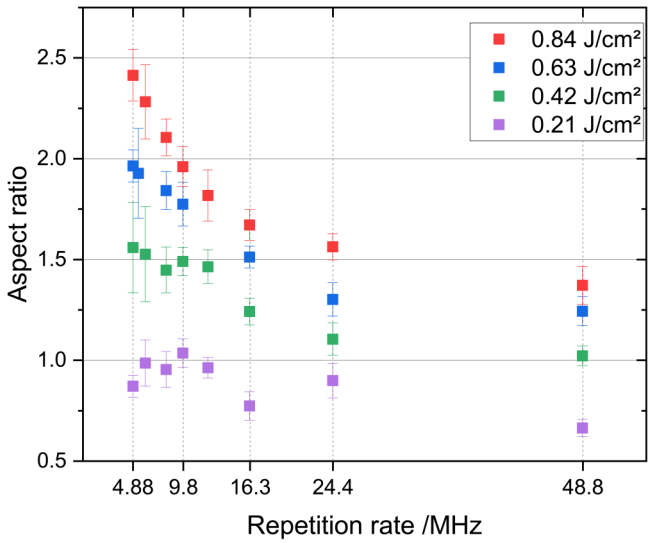

FIG. 13. Aspect ratio of the grooves depending on the repetition rate manufactured in silicon/graphite composite electrodes, ablated with a fs laser for different scanning velocities and a constant pulse-to-pulse distance of 0.1 μm.

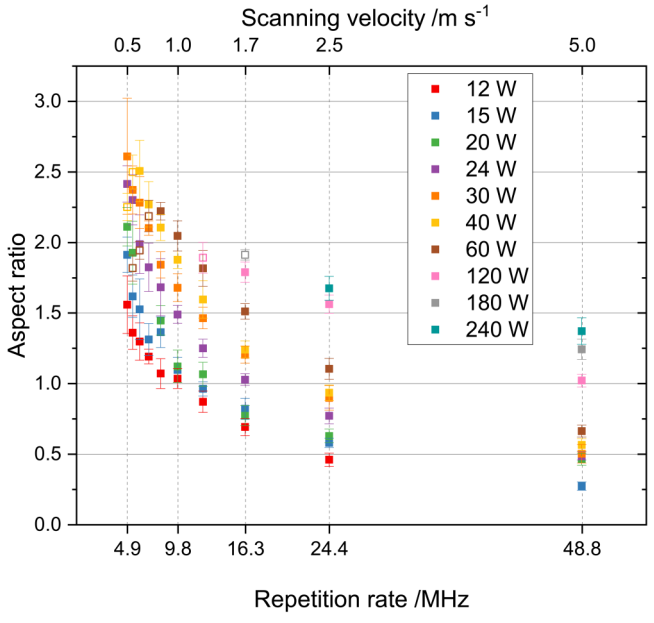

FIG. 14. Aspect ratio of the grooves depending on the repetition rate or corresponding scanning velocity manufactured in silicon/graphite composite electrodes, ablated with a fs laser for different scanning velocities and a constant pulse-to-pulse distance of 0.1 μm. Solid symbols: current collector was not reached; open symbols: current collector was reached.

powers, as shown in Fig. 14 for silicon/graphite composite electrodes and in Fig. 32 for graphite electrodes. Since it is not possible to increase the ablation depth after reaching the current collector, but there is an increase in the ablation width with a decrease in the repetition rate (equivalent to an increase in the pulse peak fluence), the aspect ratio at 40 W is reduced for graphite and silicon/graphite composite electrodes for repetition rates lower than 8.1 MHz. The highest structuring speed of 1.67 m s^{-1} for an ablation up to the current collector of both electrodes is achieved at an average laser power of 180 W and a repetition rate of 16.3 MHz. The structures have an aspect ratio of 1.9 ± 0.05. The highest aspect ratio for an ablation down to the current collector is obtained for both electrode types at 40 W and 5.4 MHz with 2.2 ± 0.1 for the graphite and 2.5 ± 0.1 for the silicon/graphite electrode. The slightly higher aspect ratio for the silicon/graphite electrode can be attributed to the slightly higher film thickness. Optimal processing parameters to achieve very high aspect ratios will be found between 30 and 40 W with a repetition rate of 4.9 MHz. This would be accompanied by reduced scanning velocities.

D. Ablation area, ablation volume, and ablation volume rate

The ablation areas and the associated ablation volume of the grooves were estimated with the four measured dimensions (upper/middle/lower width and ablation depth). The ablation area and volume are shown in Fig. 15 for silicon/graphite electrodes and in Fig. 33 for graphite electrodes. With increasing laser fluence, the ablation area and volume increase as well. At similar fluences, lower ablation areas and volumes are observed for the ablation with very high repetition rates, i.e., 24.4 and 48.8 MHz, compared to lower repetition rates, for example, 4.9 MHz.

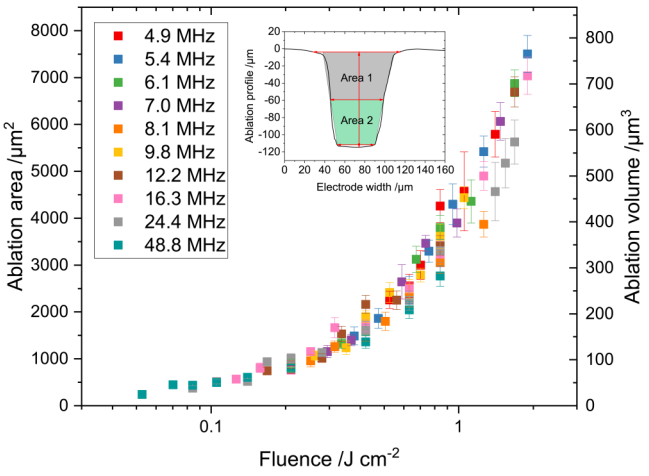

FIG. 15. Ablation area ("ablation area 1" plus "ablation area 2") of the grooves depending on the pulse peak fluence generated in silicon/graphite composite electrodes, ablated with a fs laser for different scanning velocities and a constant pulse-to-pulse distance of 0.1 μm.

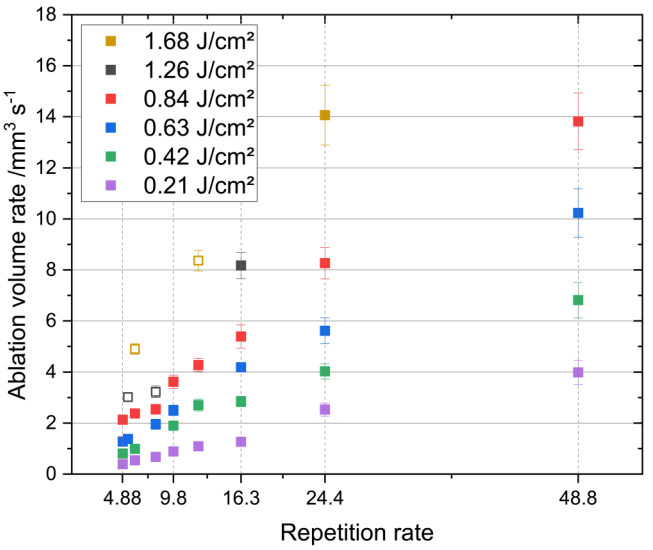

FIG. 16. Ablation volume rate in silicon/graphite composite electrodes for constant fluences depending on the repetition rate. Solid symbols: current collector was not reached; open symbols: current collector was reached.

The ablation volume rate is shown in Fig. 16 for silicon/graphite electrodes and in Fig. 34 for graphite electrodes. With increasing laser fluences, the ablation volume rate at constant repetition rates is increasing as well as the steepness of the curve. The ratio of the lower to the upper ablation area of the silicon/graphite composite electrode and the graphite electrode are shown in Figs. 35 and 36, respectively. No final statement can be made, but it seems that for the lower repetition rate range between 5.4 and 7.0 MHz, the ratio is increasing with increasing fluence. At the medium repetition rate range between 8.1 and 12.2 MHz, the ratio stays constant with increasing fluence, and at high repetition rates (24.4 and 48.8 MHz), the ratio is decreasing with the increasing repetition range. This behavior again argues for a change in the ablation mechanism and an increased influence of the plasma interaction with the increased repetition rate.

E. Electrochemical performance results

Unstructured electrodes and one exemplary laser patterned electrode with a line pitch of 200 μm containing silicon/graphite as an active material were assembled in coin cells and electrochemically tested in a rate capability measurement. The results presented as specific discharge capacities as a function of the applied C-rates are shown in Fig. 17; in Fig. 37, the total discharge capacities are shown. For the unstructured electrodes, two cells were assembled and successfully characterized. High initial capacities can be reached for one of the cells with unstructured electrodes with 485 mAh g^{-1} and for all cells with laser patterned electrodes with 505, 507, and 491 mAh g^{-1}. With increasing C-rates, the specific discharge capacity is decreasing. At a C-rate of 0.2C, a mean specific discharge capacity of 126 mAh g^{-1} is reached for the cells with

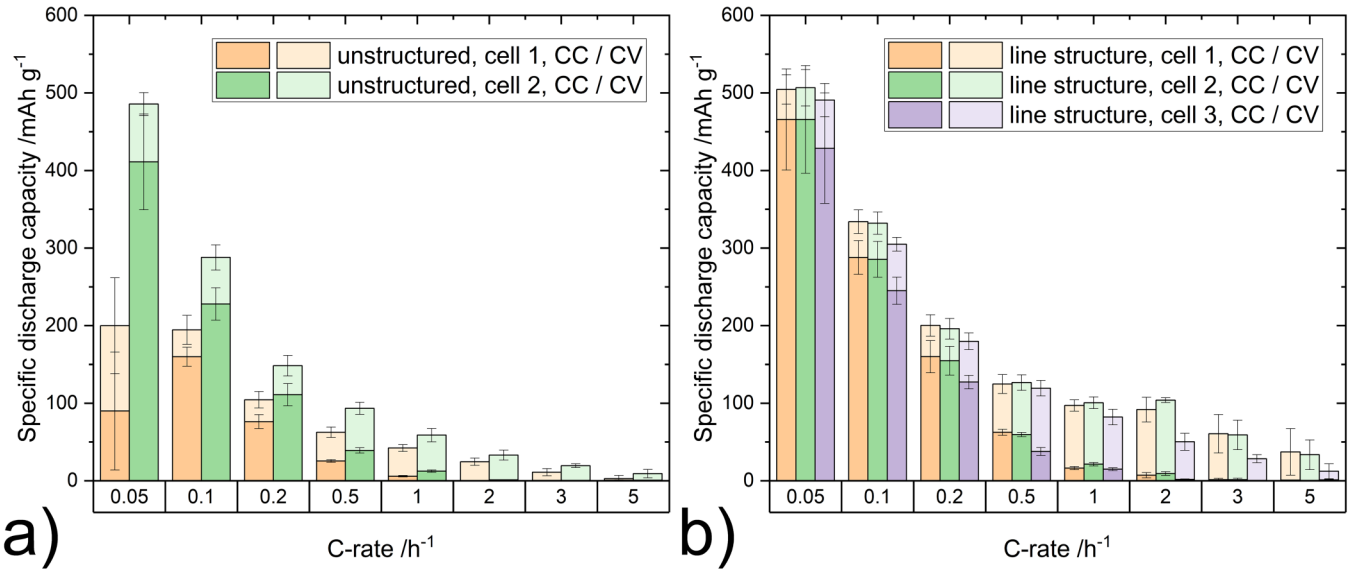

FIG. 17. Specific discharge capacities as results of electrochemical characterization of the (a) unstructured silicon/graphite composite electrodes and the (b) laser patterned electrodes assembled in coin cells versus lithium in a rate capability measurement.

unstructured electrodes, and 192 mAh g^{-1} is reached for cells with structured electrodes. At 2C, 29 mAh g^{-1} is reached for the cells with unstructured electrodes, and 82 mAh g^{-1} is reached for the structured ones, which means that there is a specific capacity increase of 283% due to laser patterning. The total discharge capacities, Fig. 37, show corresponding results. Interestingly, even though a non-negligible mass loss due to laser patterning and, therefore, a reduced amount of total active material is present in the laser patterned electrodes, higher total discharge capacities can be reached for all C-rates except 0.05C, where 6.4, 6.3, and 6.2 mAh are reached for the structured electrodes and 6.5 mAh are reached for the unstructured electrode with the best performance. The energy density can be calculated using the nominal voltage of a half cell with 0.745 V and the specific discharge capacities at 0.1C. The unstructured electrodes reach an energy density of 189 ± 26 Wh kg^{-1}, while the structured electrodes achieve an energy density of 241 ± 24 Wh kg^{-1}.

F. Aspects for laser process upscaling

For the dimensions of the Volkswagen ID.3 battery and the Tesla 4680 battery, which were thoroughly examined in Refs. 31 and 47, exemplary calculations will be presented for anode structuring. The ID.3 battery cell consists of 19 double-side coated anodes with a footprint area $w \times h$ of 512 × 97 mm^2.[31] The electrodes have a thickness t of 115.3 μm.[31] The total volume of the electrode is 5726.2592 mm^3. Taking the here used graphite electrode composition as the material, 180 W laser power could be used to structure those cells down to the current collector, using a repetition rate of 16.3 MHz and a scanning speed of 1.7 m s^{-1} (Fig. 7), resulting in a pulse peak fluence of 1.89 J cm^{-2}. The ablation volume per line is shown in Fig. 18 for this cell design (97 mm line length), the red circle indicating the chosen laser manufacturing parameters. The ablated volume per line is 0.6503 mm^3. With the ablation area A_{loss}, the width of the electrode w, and the thickness t, the relative mass loss of the electrodes m_{loss} as well as the resulting belt speed v_{belt} as a function of the line pitch p

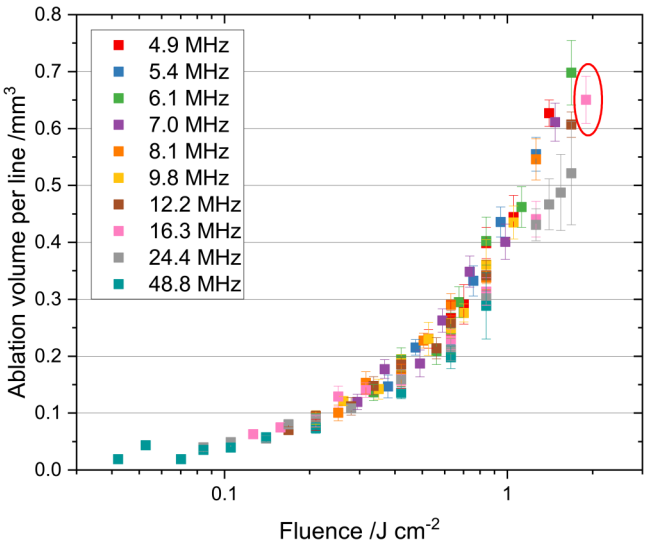

FIG. 18. Ablation volume per line for an exemplary cell design with a laser scanning line length of 97 mm, corresponding to the electrode design of a Volkswagen ID.3.

can be calculated,

$$m_{\text{loss}} = \frac{A_{\text{loss}}}{p \cdot t}, \tag{6}$$

$$v_{\text{belt}} = \frac{p \cdot v_{\text{scan}}}{h}. \tag{7}$$

The jump time of the laser is neglected. Compared to laser drilling, the amount of jumps necessary to laser pattern an electrode is orders of magnitude smaller; therefore, this assumption can be made. The result for the ID.3 is shown in Fig. 19 (red). When a limit of the mass loss to 15% it targeted, the laser line pitch has to be set to about 387 μm, and the resulting belt speed is 0.407 m min^{-1}. When using a larger pitch, for example, 1000 μm, the belt speed could be increased to 1.052 m min^{-1} and the mass loss reduced to 5.81%. The same calculations were done for the Tesla 4680 cell, which has a height h of 73 mm, a width w of 4511 mm, and a thickness t of 86.7 μm.[47] An average laser power of 180 W with a repetition rate of 24.4 MHz and a scanning speed of 2.5 m min^{-1} could be applied (pulse peak fluence of 1.262 J cm^{-2}). The resulting ablation volume per line is 0.324 mm^3. The results are shown in Fig. 19 (black). Taking a mass loss of 15% into account, the line pitch has to be set to 341 μm. The achievable belt speed is 0.702 m min^{-1}. When the pitch is increased to 1000 μm, the belt speed can be increased to 2.055 m min^{-1} and the ablated volume can be decreased to 5.12%. The laser patterning process has to be further accelerated to match the belt speed of the industrial requirements. The usage of beam splitters (either conventional optics or diffractive optical elements) could be used to further increase the processing speed. Diffractive optical elements for beam splitting (1 × 5) and for beam shaping were applied for laser patterning of graphite electrodes in Ref. 48, and a fivefold increase in process speed was achieved. In Ref. 49, a beam shaper and a beam splitter were applied to pattern graphite electrodes, and the scanning speed was increased sevenfold, while the processing speed compared to the experimental setup without diffractive optical elements was increased 35-fold. The development of high-power ultrafast laser sources with average laser powers of 1 kW or even more is already underway, for example, in two European Union's Horizon 2020 projects.[50,51] With those laser sources, the fast laser patterning of electrodes could be made feasible. Those high-power laser beam with a usable power of 1 kW could be split into several beamlets, for example, into a five equidistant beamlet, each having a total laser power of 200 W. Considering the expected diffraction losses of 5%, the laser power at the working pane is 190 W per beamlet. A repetition rate of 24.4 MHz and a scanning speed of 2.5 m min^{-1} could be used to structure the Tesla 4680 graphite electrode with one scan down to the current collector; with a line pitch of 1000 μm, the belt speed can be increased to 10.275 m min^{-1}.

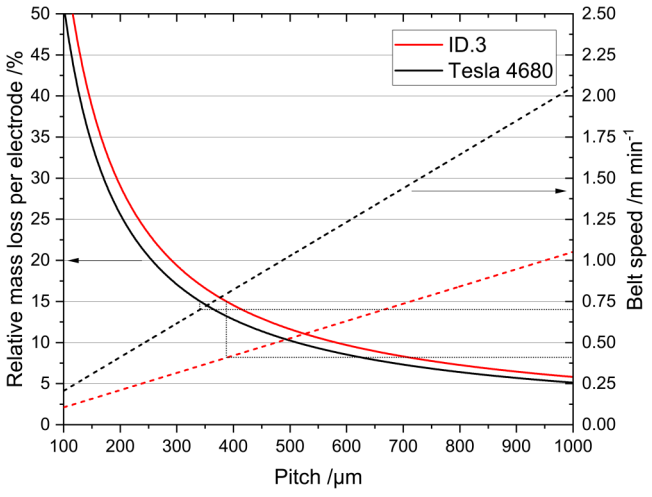

FIG. 19. Relative mass loss per electrode and belt speed as a function of line pitch for an ID.3 cell (electrode width 512 mm, height 97 mm, thickness 115.3 μm, laser parameters: 180 W, 16.3 MHz repetition rate, 1.7 m s^{-1} scanning velocity, and 1.89 J cm^{-2} laser fluence) and a Tesla 4680 cell (electrode width 4511 mm, height 73 mm, thickness 86.7 μm, laser parameters: 180 W, 24.4 MHz repetition rate, 2.5 m s^{-1} scanning velocity, and 1.26 J cm^{-2} laser pulse peak fluence).

IV. CONCLUSIONS

Using high-power, high repetition rate ultrafast lasers, the laser-direct write ablation behavior of thick silicon/graphite composite electrodes and graphite electrodes was investigated. Different energy densities, repetition rates, and pulse-to-pulse distances were applied. For the experimental setup with a Gaussian beam shape, two ablation regimes of the ablation depth could be identified depending on the pulse peak fluence. The two ablation regimes are distinguished from each other by transition from ablation without thermal influence at low pulse peak fluences and ablation with thermal influence at high pulse peak fluences. With increasing repetition rates, the ablation at a constant pulse peak fluence is reduced. This can be observed more prominently for higher pulse peak fluences. The ablation depth depending on the repetition rate is increasing with increasing laser power and decreasing with increasing repetition rates. The ablation width is also increasing with increasing pulse peak fluences or laser powers, just as it increases with increasing repetition rates at constant pulse peak fluences. The laser pulses interact with the evolving plasma plume or material vapor plume of the respective preceding laser pulse. High electron densities lead to increased plasma frequencies, and the absorption of the laser energy in the plasma is enhanced. The laser beam is dispersed in the plasma, and the coupling of the laser beam into the material is hindered. An important measurement for the quality of laser patterning is the aspect ratio, which is identified to be the highest for a repetition rate of 4.9 MHz and a fluence of 1.05 J cm^{-2} or a power of 30 W with 2.61. When too low powers or fluences are used, the electrode cannot be structured down to the current collector, but when the fluence or laser power is chosen to be too high, the current collector is exposed, resulting in a reflexion of the laser beam and re-coupling in the electrode material, which, therefore, dramatically increases the ablation widths, resulting in a lowered aspect ratio and a high material loss. The aspect ratio decreases with increasing repetition rates at constant fluences or powers. With the development of high-power USP laser sources in the kW regime, the usage of more than one laser source or a laser source with longer pulse lengths (in the picosecond regime), the laser patterning process can be scaled to achieve desirable belt speeds in the range of several meters per minute.

ACKNOWLEDGMENTS

This research was funded by the Federal Ministry of Education and Research (BMBF), project NextGen-3DBat, Grant No. 03XP0198F. The authors would like to acknowledge Ulrich Rädel (Topag AG) for providing beam shaping and beam splitting optics and Keming Du (EdgeWave GmbH) for providing the laser source.

AUTHOR DECLARATIONS

Conflict of Interest

The authors have no conflicts to disclose.

Author Contributions

Alexandra Meyer: Conceptualization (equal); Data curation (equal); Formal analysis (equal); Methodology (equal); Validation (equal); Visualization (equal); Writing – original draft (equal). **Yannic Sterzl:** Conceptualization (equal); Data curation (equal); Formal analysis (equal); Investigation (equal); Methodology (equal); Validation (equal); Visualization (equal). **Wilhelm Pfleging:** Conceptualization (equal); Funding acquisition (equal); Project administration (equal); Resources (equal); Supervision (equal); Writing – review & editing (equal).

DATA AVAILABILITY

The data that support the findings of this study are available within the article.

APPENDIX: ADDITIONAL RESULTS REGARDING CHEMICAL COMPOSITION, ABLATION CHARACTERISTICS, AND ELECTROCHEMICAL BEHAVIOR

Figures 20–37.

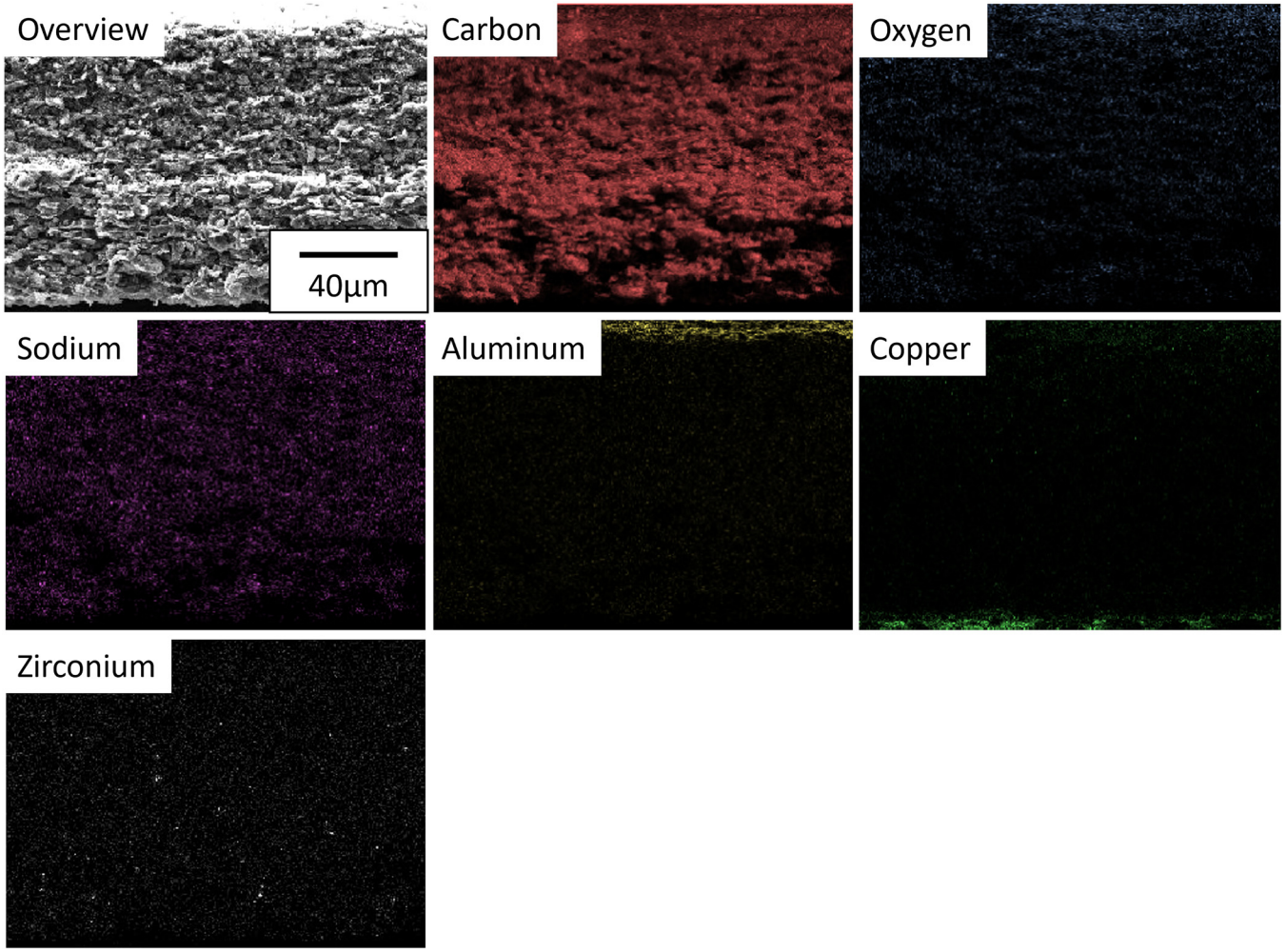

FIG. 20. Results of the energy-dispersive x-ray spectrometry performed on the cross-sectional view of the electrode.

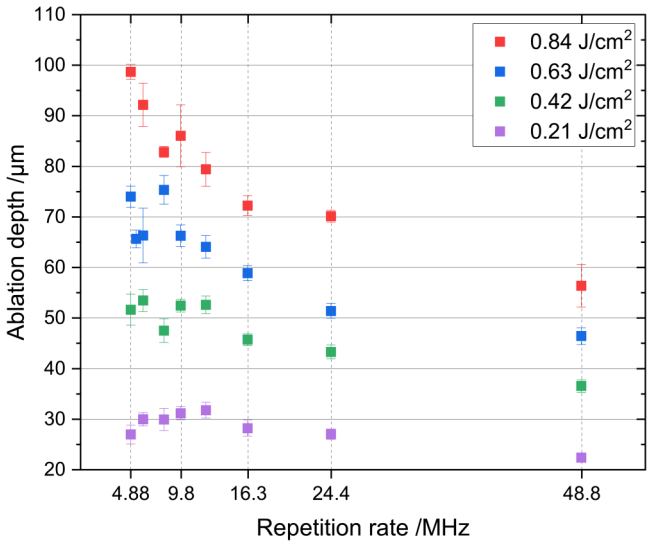

FIG. 21. Ablation depth depending on the repetition rate at constant fluences for graphite ablated with a fs laser for different scanning velocities and a constant pulse-to-pulse distance of 0.1 μm.

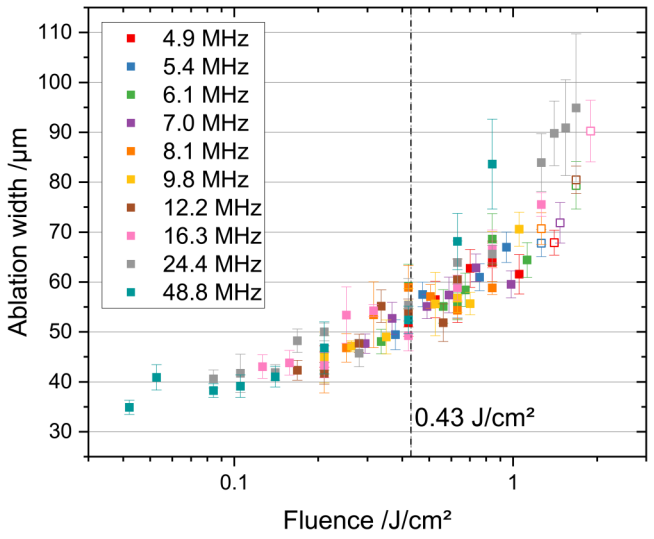

FIG. 23. Upper ablation width depending on the pulse peak fluence for graphite electrodes, ablated with a fs laser for different scanning velocities and a constant pulse-to-pulse distance of 0.1 μm. Solid symbols: current collector was not reached; open symbols: current collector was reached.

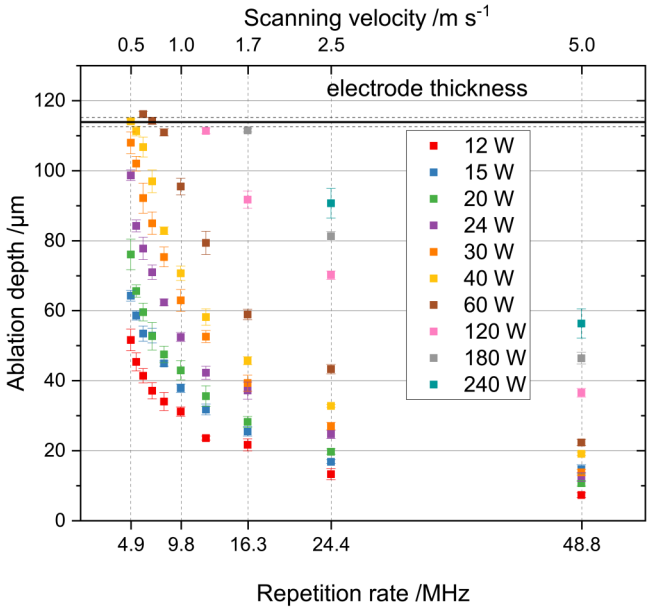

FIG. 22. Ablation depth for constant laser powers as a function of repetition rate or corresponding scanning velocity for graphite electrodes, ablated with a fs laser for different scanning velocities and a constant pulse-to-pulse distance of 0.1 μm.

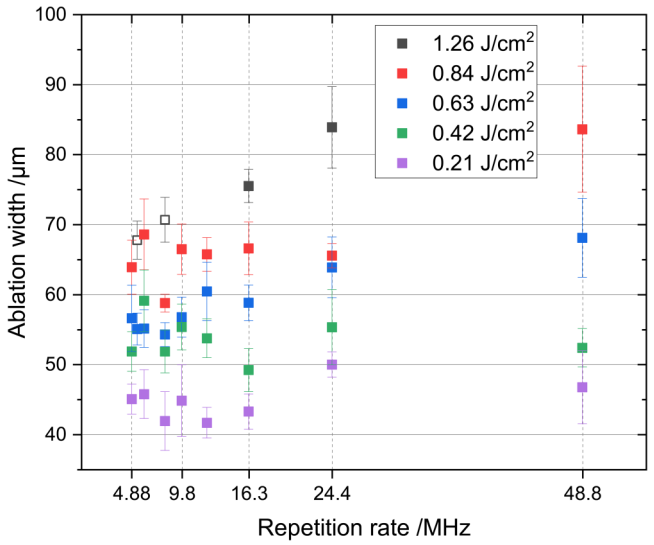

FIG. 24. Upper ablation width depending on the repetition rate for constant pulse peak fluence for graphite electrodes, ablated with a fs laser for different scanning velocities and a constant pulse-to-pulse distance of 0.1 μm. Solid symbols: current collector was not reached; open symbols: current collector was reached.

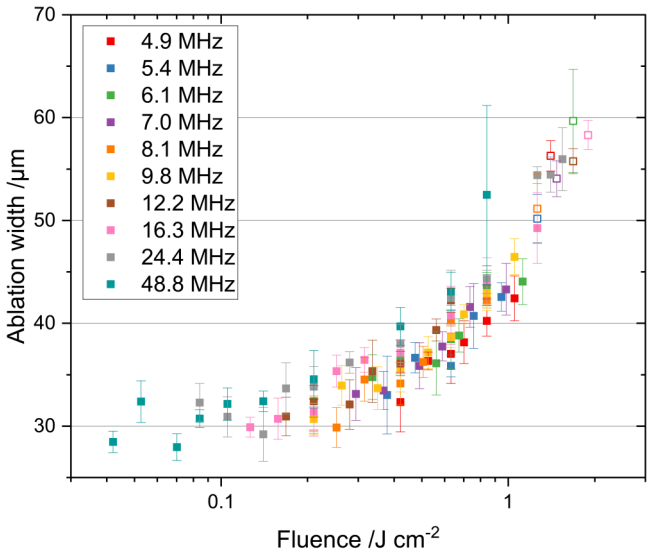

FIG. 25. Middle ablation width depending on the repetition rate for constant pulse peak fluence for graphite electrodes, ablated with a fs laser for different scanning velocities and a constant pulse-to-pulse distance of 0.1 μm. Solid symbols: current collector was not reached; open symbols: current collector was reached.

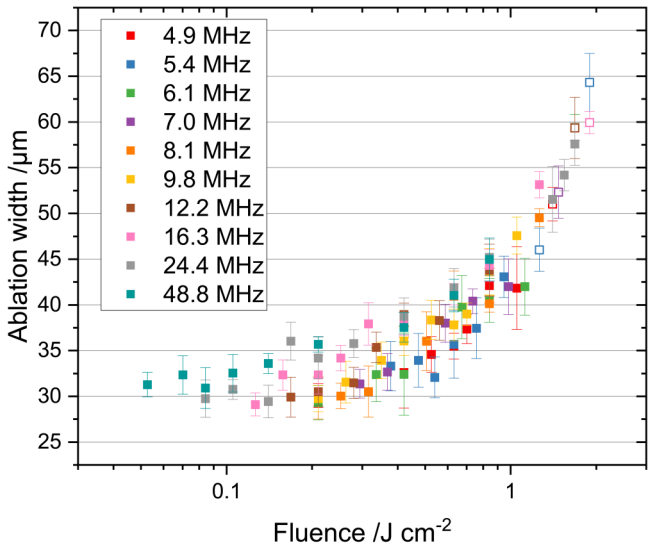

FIG. 27. Middle ablation width depending on the pulse peak fluence for silicon/graphite composite electrodes, ablated with a fs laser for different scanning velocities and a constant pulse-to-pulse distance of 0.1 μm. Solid symbols: current collector was not reached; open symbols: current collector was reached.

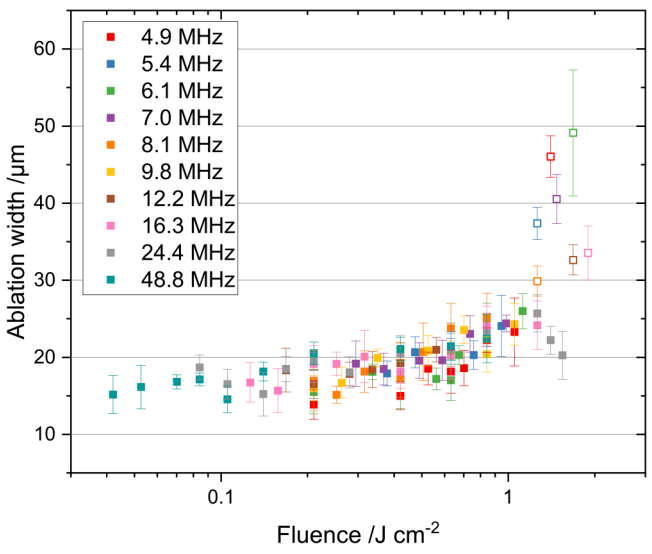

FIG. 26. Lower ablation width depending on the repetition rate for constant pulse peak fluence for graphite electrodes, ablated with a fs laser for different scanning velocities and a constant pulse-to-pulse distance of 0.1 μm. Solid symbols: current collector was not reached; open symbols: current collector was reached.

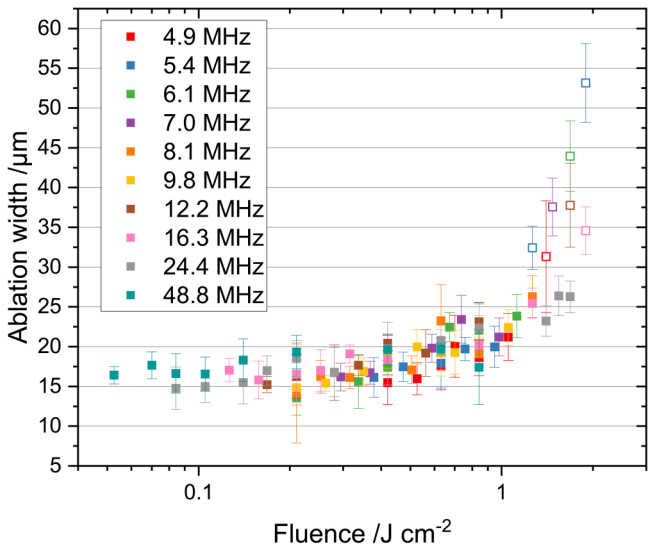

FIG. 28. Lower ablation width depending on the pulse peak fluence for silicon/graphite composite electrodes, ablated with a fs laser for different scanning velocities and a constant pulse-to-pulse distance of 0.1 μm. Solid symbols: current collector was not reached; open symbols: current collector was reached.

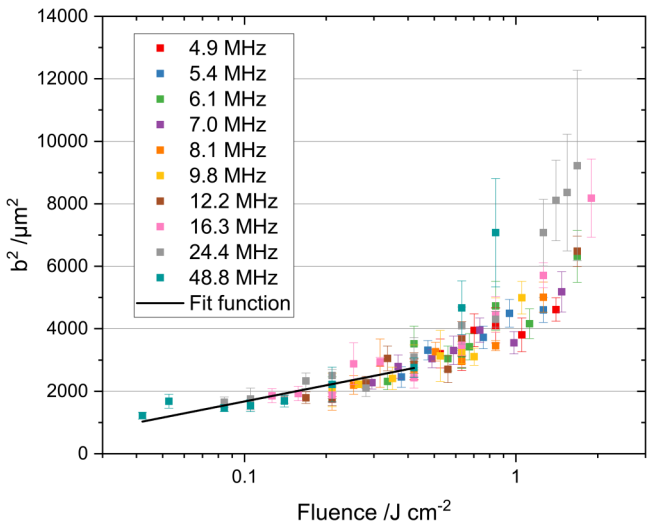

FIG. 29. Squared upper ablation width and fitting function for fluences under 0.43 J cm^{-2} depending on the repetition rate for constant pulse peak fluence for graphite electrodes, ablated with a fs laser for different scanning velocities and a constant pulse-to-pulse distance of 0.1 μm.

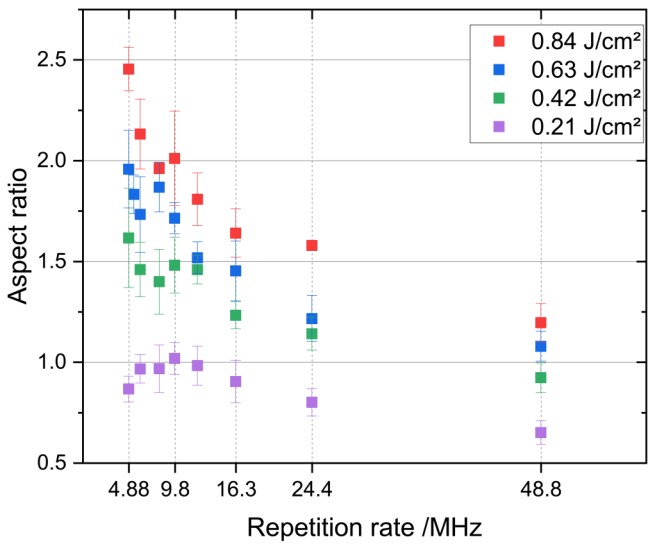

FIG. 31. Aspect ratio of the grooves depending on the repetition rate manufactured in graphite electrodes ablated with a fs laser for different scanning velocities and a constant pulse-to-pulse distance of 0.1 μm. Solid symbols: current collector was not reached; open symbols: current collector was reached.

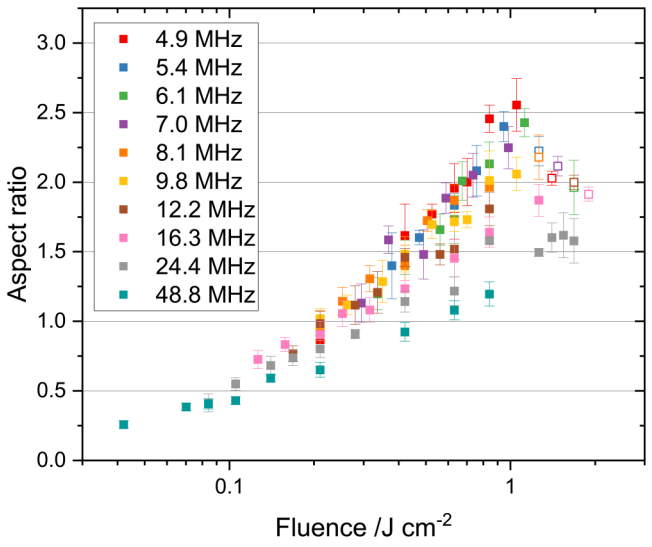

FIG. 30. Aspect ratio of the grooves depending on the pulse peak fluence manufactured in graphite electrodes, ablated with a fs laser for different scanning velocities and a constant pulse-to-pulse distance of 0.1 μm. Solid symbols: current collector was not reached; open symbols: current collector was reached.

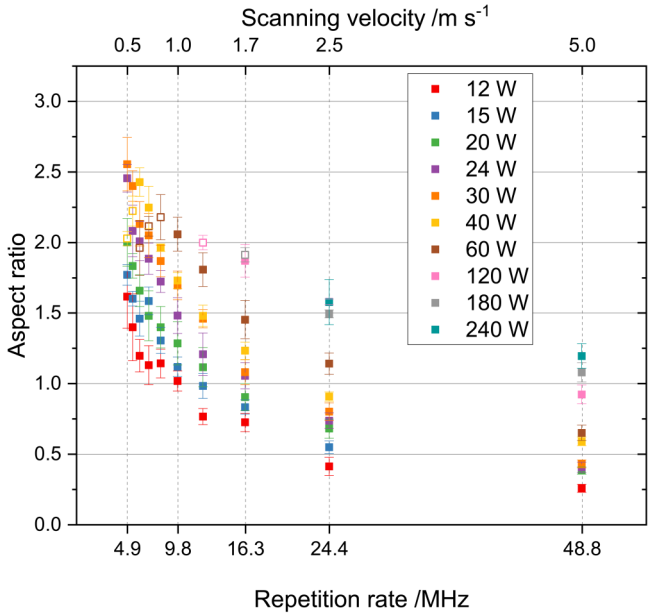

FIG. 32. Aspect ratio of the grooves depending on the repetition rate or corresponding scanning velocity manufactured in graphite electrodes, ablated with a fs laser for different scanning velocities and a constant pulse-to-pulse distance of 0.1 μm. Solid symbols: current collector was not reached; open symbols: current collector was reached.

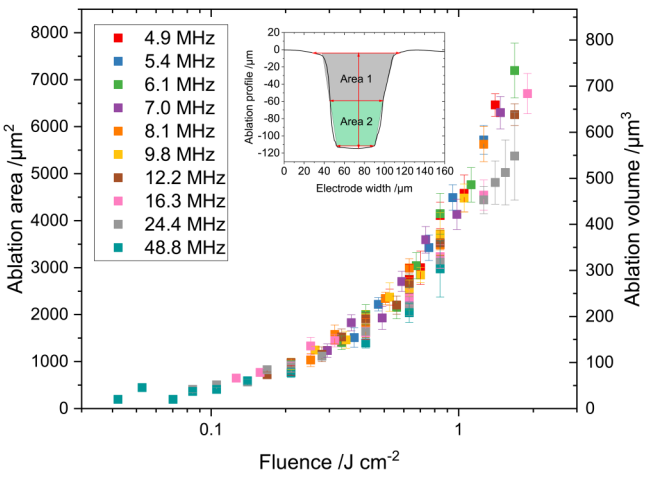

FIG. 33. Ablation area and volume of the grooves depending on the pulse peak fluence manufactured in graphite electrodes, ablated with a fs laser for different scanning velocities and a constant pulse-to-pulse distance of 0.1 μm.

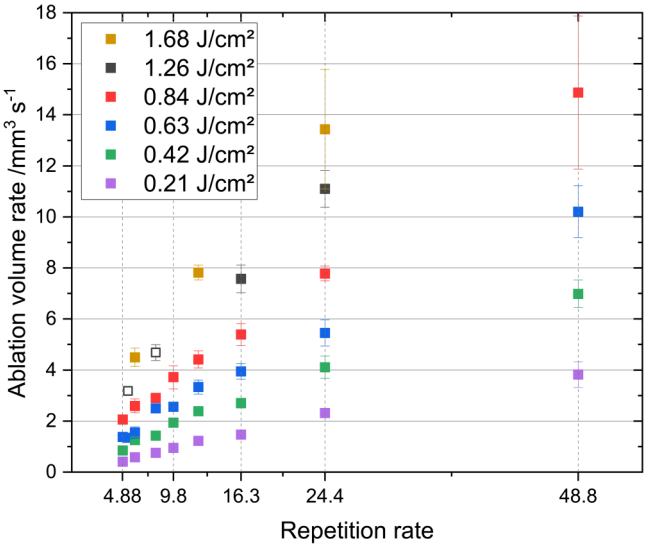

FIG. 34. Ablation volume rate in graphite electrodes for constant fluences depending on the repetition rate. Solid symbols: current collector was not reached; open symbols: current collector was reached.

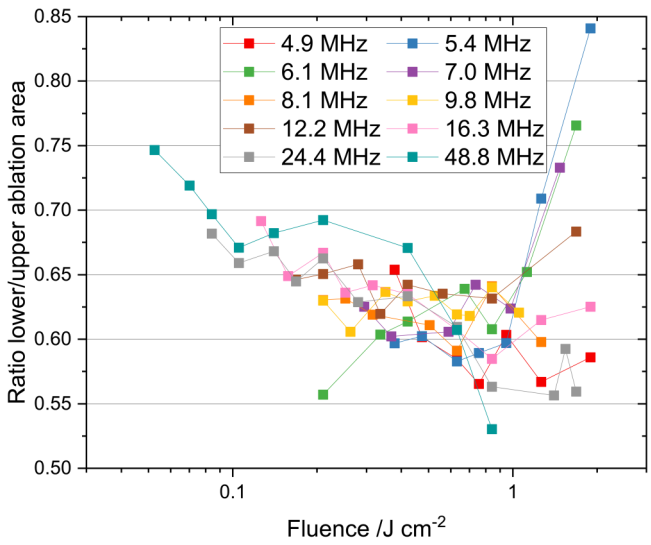

FIG. 35. Ratio of the lower to the upper ablation area of silicon/graphite composite electrodes.

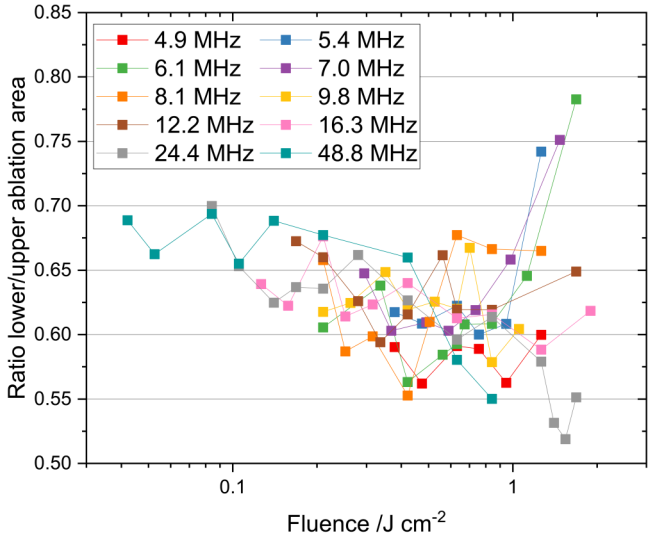

FIG. 36. Ratio of the lower to the upper ablation area of graphite electrodes.

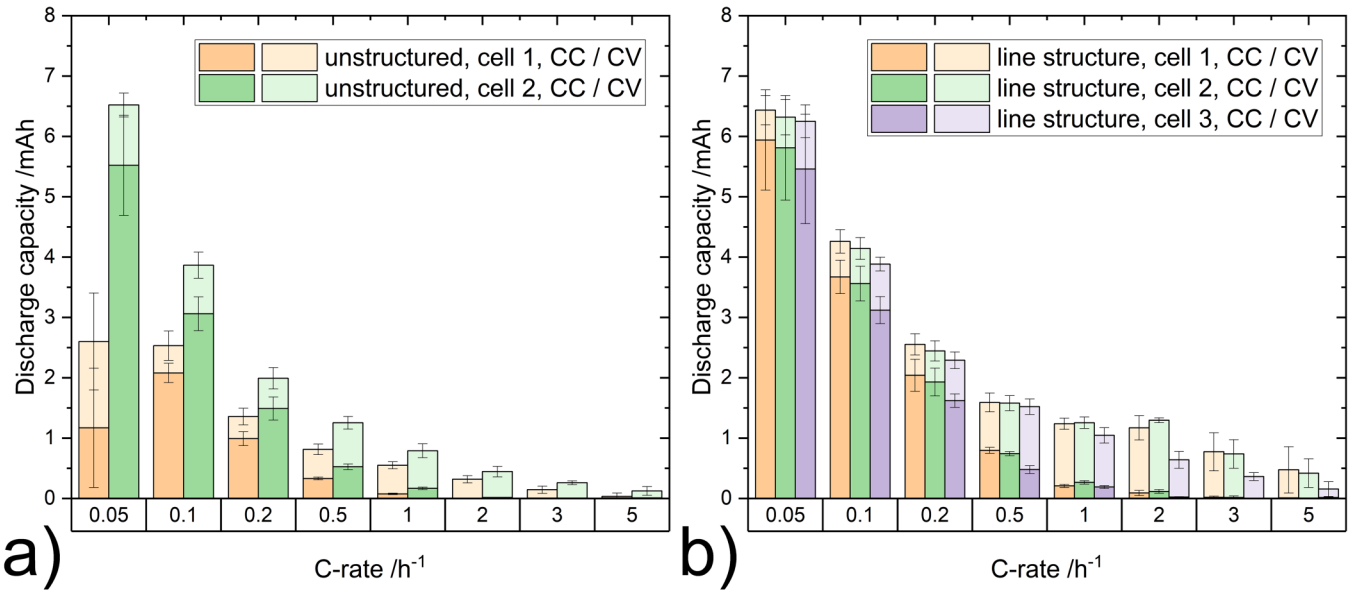

FIG. 37. Discharge capacities as results of electrochemical characterization of the (a) unstructured silicon/graphite composite electrodes and the (b) laser patterned electrodes assembled in coin cells versus lithium in a rate capability measurement.

REFERENCES

[1]W. Pfleging, "Recent progress in laser texturing of battery materials: A review of tuning electrochemical performances, related material development, and prospects for large-scale manufacturing," Int. J. Extrem. Manuf. **3**, 012002 (2021).

[2]Batteries Europe, see https://batterieseurope.eu/results/technology-roadmap/technology-roadmap-2021/ for "Roadmap on Advanced Materials for Batteries."

[3]W. Pfleging, "A review of laser electrode processing for development and manufacturing of lithium-ion batteries," Nanophotonics **7**, 549–573 (2018).

[4]W. Pfleging, R. Kohler, and J. Pröll, "Laser generated microstructures in tape cast electrodes for rapid electrolyte wetting: New technical approach for cost efficient battery manufacturing," in *Laser-Based Micro- and Nanoprocessing VIII*, edited by U. Klotzbach, K. Washio, and C. B. Arnold (SPIE, Bellingham, WA, 2014), p. 89680B.

[5]W. Pfleging and J. Pröll, "A new approach for rapid electrolyte wetting in tape cast electrodes for lithium-ion batteries," J. Mater. Chem. A **2**, 14918–14926 (2014).

[6]M. N. Obrovac and L. Christensen, "Structural changes in silicon anodes during lithium insertion/extraction," Electrochem. Solid-State Lett. **7**, A93 (2004).

[7]J. Asenbauer, T. Eisenmann, M. Kuenzel, A. Kazzazi, Z. Chen, and D. Bresser, "The success story of graphite as a lithium-ion anode material—Fundamentals, remaining challenges, and recent developments including silicon (oxide) composites," Sustain. Energy Fuels **4**, 5387–5416 (2020).

[8]Y. Zheng, H. J. Seifert, H. Shi, Y. Zhang, C. Kübel, and W. Pfleging, "3D silicon/graphite composite electrodes for high-energy lithium-ion batteries," Electrochim. Acta **317**, 502–508 (2019).

[9]H. Shi, X. Liu, R. Wu, Y. Zheng, Y. Li, X. Cheng, W. Pfleging, and Y. Zhang, "In situ SEM observation of structured Si/C anodes reactions in an ionic-liquid-based lithium-ion battery," Appl. Sci. **9**, 956 (2019).

[10]A. Meyer, F. Ball, and W. Pfleging, "The effect of silicon gradae and electrode architecture on the performance of advanced anodes for next generation lithium-ion cells," Nanomaterials **11**, 3448 (2021).

[11]J. B. Habedank, J. Kriegler, and M. F. Zach, "Enhanced fast charging and reduced lithium-plating by laser-structured anodes for lithium-ion batteries," J. Electrochem. Soc. **166**, A3940–A3949 (2019).

[12]M. Yamada, N. Soma, M. Tsuta, S. Nakamura, N. Ando, and F. Matsumoto, "Development of a roll-to-roll high-speed laser micro processing machine for preparing through-holed anodes and cathodes of lithium-ion batteries," Int. J. Extrem. Manuf. **5**, 035004 (2023).

[13]W. Pfleging, P. Gotcu, P. Smyrek, Y. Zheng, J. K. Lee, and H. J. Seifert, in *Laser Micro-Nano-Manufacturing and 3D Microprinting*, edited by A. Hu (Springer International, Cham, 2020), Vol. 309, pp. 313.

[14]S. Nolte, C. Momma, H. Jacobs, A. Tünnermann, B. N. Chichkov, B. Wellegehausen, and H. Welling, "Ablation of metals by ultrashort laser pulses," J. Opt. Soc. Am. B **14**, 2716–2722 (1997).

[15]J. B. Habedank, J. Endres, P. Schmitz, M. F. Zaeh, and H. P. Huber, "Femtosecond laser structuring of graphite anodes for improved lithium-ion batteries: Ablation characteristics and process design," J. Laser Appl. **30**, 32205 (2018).

[16]M. Kouli, M. W. Kandula, and K. Dilger, "Laser-material-interactions between ultrashort pulse lasers and electrodes for lithium-ion batteries during micro-structuring the electrode surface," in *Laser-Based Micro- and Nanoprocessing XV*, edited by U. Klotzbach, R. Kling, and A. Watanabe (SPIE, Bellingham, WA, 2021), p. 46.

[17]A. Kwade, W. Haselrieder, R. Leithoff, A. Modlinger, F. Dietrich, and K. Droeder, "Current status and challenges for automotive battery production technologies," Nat. Energy **3**, 290–300 (2018).

[18]H. H. Heimes, A. Kampker, C. Lienemann, M. Locke, C. Offermanns, S. Michaelis, and E. Rahimzei, *Lithium-Ion Battery Cell Production Process* (PEM der RWTH Aachen University, DVMA, Aachen, Frankfurt am Main, 2018).

[19]D. L. Wood, M. Wood, J. Li, Z. Du, R. E. Ruther, K. A. Hays, N. Muralidharan, L. Geng, C. Mao, and I. Belharouak, "Perspectives on the relationship between materials chemistry and roll-to-roll electrode manufacturing for high-energy lithium-ion batteries," Energy Stor. Mater. **29**, 254–265 (2020).

[20]W. B. Hawley and J. Li, "Electrode manufacturing for lithium-ion batteries—Analysis of current and next generation processing," J. Energy Stor. **25**, 100862 (2019).
[21]Z. Du, C. J. Janke, J. Li, and D. L. Wood, "Speed electron beam curing of thick electrode for high energy density Li-ion batteries," Green Energy Environ. **4**, 375–381 (2019).
[22]J. Li, J. Fleetwood, W. B. Hawley, and W. Kays, "Materials to cell: State-of-the-art and prospective technologies for lithium-ion battery electrode processing," Chem. Rev. **122**, 903–956 (2022).
[23]Y. Zheng, L. Pfäffl, H. J. Seifert, and W. Pfleging, "Distribution in structured graphite anodes investigated by laser-induced breakdown spectroscopy," Appl. Sci. **9**, 4218 (2019).
[24]P. Zhu, H. J. Seifert, and W. Pfleging, "The ultrafast laser ablation of Li (Ni0.6Mn0.2Co0.2)O2 electrodes with high mass loading," Appl. Sci. **9**, 4067 (2019).
[25]Y. Zheng, P. Smyrek, J.-H. Rakebrandt, C. Kübel, H. J. Seifert, and W. Pfleging, "Silicon-based 3D electrodes for high power lithium-ion battery," in *IEEE Conference*, *Shanghai, China, 7–11 August 2017* (IEEE, New York, 2017).
[26]Y. Zheng, P. Smyrek, J.-H. Rakebrandt, C. Kübel, H. J. Seifert, and W. Pfleging, "Fabrication and characterization of silicon-based 3D electrodes for high-energy lithium-ion batteries," in *Laser-Based Micro- and Nanoprocessing XI*, edited by U. Klotzbach, K. Washio, and R. Kling (SPIE, Bellingham, WA, 2017), p. 100920L.
[27]M. Mangang, H. J. Seifert, and W. Pfleging, "Influence of laser pulse duration on the electrochemical performance of laser structured LiFePO4 composite electrodes," J. Power Sources **304**, 24–32 (2016).
[28]W. Pfleging, Y. Zheng, M. Mangang, M. Bruns, and P. Smyrek, "Laser processes and analytics for high power 3D battery materials," in *Frontiers in Ultrafast Optics*: *Biomedical*, *Scientific*, *and Industrial Applications XVI*, edited by A. Heisterkamp, P. R. Herman, M. Meunier, and S. Nolte (SPIE, Bellingham, WA, 2016), p. 974013.
[29]J. Pröll, H. Kim, A. Piqué, H. J. Seifert, and W. Pfleging, "Laser-printing and femtosecond-laser structuring of LiMn2O4 composite cathodes for Li-ion microbatteries," J. Power Sources **255**, 116–124 (2014).
[30]Y. Sterzl and W. Pfleging, "Extending the 3D-battery concept—Large areal ultrashort pulsed laser structuring of multilayered electrode coatings," in *Laser-Based Micro- and Nanoprocessing XVII*, edited by R. Kling, W. Pfleging, and A. Watanabe (SPIE, Bellingham, WA, 2023).
[31]F. J. Günter and N. Wassiliadis, "State of the art of lithium-ion pouch cells in automotive applications: Cell teardown and characterization," J. Electrochem. Soc. **169**, 030515 (2022).
[32]F. Han, D. Xiong, Q. Wang, B. Shao, and M. Chen, "Thermal properties of carboxymethylcellulose and methyl methacrylate graft copolymers," J. Macromol. Sci. **52**, 1242–1249 (2013).
[33]S. Mishra, N. G. Shimpi, and U. D. Patil, "Effect of nano CaCO3 on thermal properties of styrene butadiene rubber (SBR)," J. Polym. Res. **14**, 449–459 (2007).
[34]M. L. V. Gayler, "Melting point of high-purity silicon," Nature **142**, 478 (1938).
[35]J. Abrahamson, "Graphite sublimation temperatures, carbon arcs and crystallite erosion," Carbon **12**, 111–141 (1974).
[36]A. Slocombe and L. Li, "Laser ablation machining of metal/polymer composite materials," Appl. Surf. Sci. **154–155**, 617–621 (2000).
[37]M. D. Shirk and P. A. Molian, "Ultra-short pulsed laser ablation of highly oriented pyrolytic graphite," Carbon **39**, 1183–1193 (2001).
[38]T. Lippert and J. T. Dickinson, "Chemical and spectroscopic aspects of polymer ablation: Special features and novel directions," Chem. Rev. **103**, 453–486 (2003).
[39]M.-C. Chuang and A. C. Tam, "On the saturation effect in the picosecond near ultraviolet laser ablation of polyimide," J. Appl. Phys. **65**, 2591–2595 (1989).
[40]K. Wiesemann, "A short introduction to plasma physics," in *CAS - CERN Acelerator School*, edited by R. Bailey (CAS, Senec, Slovakia, 2012).
[41]S. I. Kudryashov, A. A. Ionin, S. V. Makarov, N. N. Mel'nik, L. V. Seleznev, and D. V. Sinitsyn, "Femtosecond laser ablation of carbon: From spallation to formation of hot critical plasma," AIP Conf. Proc. **1464**, 244–255 (2012).
[42]W. Bao, N. Zhang, P. Feng, H. Wu, and X. Zhu, "Time and species dependent ambient air's effects on carbon clusters generated during femtosecond laser ablation of highly oriented pyroliti graphite," Eur. Phys. J. D **69**, 270 (2015).
[43]H.-J. Hagemann, W. Gudet, and C. Kunz, "Optical constants from the far infrared to the X-ray region: Mg, Al, Cu, Ag, Bi, and Al_2O_3," Deutsches Elektronen-Synchroton DESY, DESY-report SR-74/7 (1974).
[44]E. D. Palik, *Handbook of Optical Constants in Solids* (Academic, Maryland, 1988).
[45]D. Park and D. Lee, "Effect of fluence and multi-pass on groove morphology and process efficiency of laser structuring for 3D electrodes of lithium-ion batteries," Materials **14**, 1283 (2021).
[46]S. Xiao, E. L. Gurevich, and A. Ostendorf, "Incubation effect and its influence on laser patterning of ITO thin film," Appl. Phys. A **107**, 333–338 (2012).
[47]A. Frank, J. Sturm, M. Steinhardt, A. Rheinfeld, and A. Jossen, "Impact of current collector design and cooling topology on fast charging of cylindrical lithium-ion batteries," ECS Adv. **1**, 040502 (2022).
[48]A. Meyer, Y. Sterzl, U. Rädel, S. Xiao, M. Zenz, D. Schwab, and W. Pfleging, "Laser structuring of electrodes in roll-to-roll environment using multi-beam processing: Process upscaling and its perspective," in *Laser-Based Micro- and Nanoprocessing XVII*, edited by R. Kling, W. Pfleging, and A. Watanabe (SPIE, Bellingham, WA, 2023), p. 24.
[49]A. Meyer, Y. Sterzl, S. Xiao, U. Rädel, and W. Pfleging, "Ablation behaviour of electrode materials during high power and high repetition rate laser structuring," in *Laser-Based Micro- and Nanoprocessing XVI*, edited by R. Kling and A. Watanabe (SPIE, Bellingham, WA, 2022), p. 26.
[50]Fraunhofer Gesellschaft zur Förderung der angewandten Forschung, Cordis Project, see https://cordis.europa.eu/project/id/825201.
[51]FUNDACION TEKNIKER, see http://multipoint-project.eu/ for "Multipoint Project."